CHAPTER 4

Curvature Analysis

4.1 Introduction

Due to the elasticity of tooth surfaces, the instantaneous contact point of the meshing tooth surfaces is spread over an elliptical area under the load. The dimensions and orientations of the contact ellipses depend on the principal curvatures of the contact surfaces. one of the application of curvature analysis is to investigate the tooth undercutting when the envelope surfaces are generated. The tooth undercutting will occur if the normal curvature of the generating surface is smaller than that of the generated surface.

Relationships between the principal curvatures and directions of the surfaces were proposed by Litvin [22]. The approach of curvature analysis proposed by Litvin can determine the principal curvatures and directions of the generated surfaces without the knowledge of the complex tooth surfaces. He investigated the relationships of the principal curvatures and directions for tooth surfaces in point contact and line contact, but these tooth surfaces are the envelope to one-parameter family of surfaces.

The motion of the hob cutter surfaces that envelope the surface of the curvilinear-tooth gear is considered as the two-parameter motion of a rigid body. In this case, the hob cutter surface and tooth surface are in point contact and the tooth surface of the curvilinear-tooth gear is represented by four related parameters. Therefore, it is difficult to calculate the curvatures of complex tooth surfaces by using differential geometry method. In this chapter, equations related the principal curvatures and directions of the two surfaces are formulated.

4.2 Relations Between Relative Velocity

The generating surface Σ_1 is a regular surface and is represented in coordinate system $S_1(X_1, Y_1, Z_1)$ as:

$$\mathbf{r}_1^{(1)}(l, \phi) \in C^1, \quad \frac{\partial \mathbf{r}_1^{(1)}}{\partial l} \times \frac{\partial \mathbf{r}_1^{(1)}}{\partial \phi} \neq 0, \quad (l, \phi) \in E, \tag{4.1}$$

where l and ϕ are surface parameters of surface Σ_1. The normal to surface Σ_1 is represented as follows:

$$\mathbf{N}_1^{(1)} = \frac{\partial \mathbf{r}_1^{(1)}}{\partial l} \times \frac{\partial \mathbf{r}_1^{(1)}}{\partial \phi}. \tag{4.2}$$

The surface Σ_2 as the envelope to the two-parameter family of surface Σ_1 can be represented as follows:

$$\mathbf{r}_2^{(2)}(l, \phi, \theta, \psi) = \mathbf{M}_{21}(\theta, \psi)\mathbf{r}_1^{(1)}(l, \phi), \tag{4.3}$$

$$\mathbf{n}^{(1)} \cdot \mathbf{V}^{(12,\theta)} = f(l, \phi, \theta, \psi) = 0, \tag{4.4}$$

and $$\mathbf{n}^{(1)} \cdot \mathbf{V}^{(12,\psi)} = g(l, \phi, \theta, \psi) = 0, \tag{4.5}$$

where Matrix $\mathbf{M}_{21}$ represents the coordinate transformation from coordinate system $S_1(X_1, Y_1, Z_1)$ to $S_2(X_2, Y_2, Z_2)$. θ and ψ depict two independent parameters which determined the relative motion between the tool surface Σ_1 and envelope Σ_2. $\mathbf{n}^{(1)}$ represents the unit normal of tool surface Σ_1. The symbol $\mathbf{V}^{(12,j)}$ represents the relative velocity of contact point when parameter $j = \theta$ (or ψ) is varied and parameter ψ (or θ) is fixed. Equations (4.4) and (4.5) that relate the parameters l, ϕ, θ, and ψ are called equations of meshing.

Figure 4.1 reveals the relationship among coordinate systems for the generation mechanism with two-parameter motion. The motion of the hob cutter surface Σ_1 can

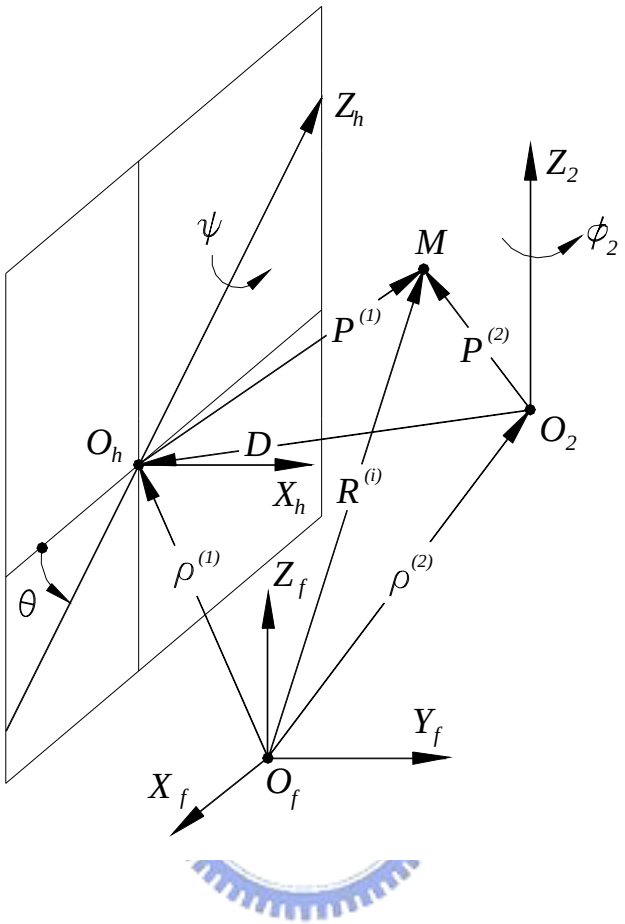

Fig. 4.1 Simulation of a generation mechanism with two-parameter motion

be represented by two independent parameters, rotational angles θ and ψ, while axes Z_h and X_h are the rotational axis of the surface Σ_1, respectively. Axis Z_2 represents the rotational axis of the gear tooth surface Σ_2. Axes Z_h and X_h are intersected at Point O_h. The point M is a common point to both rotating surfaces. $\mathbf{P}^{(1)}$ is the position vector drawn form point O_h to point M. $\mathbf{P}^{(2)}$ represents the position vector drawn to point M from an arbitrary point on the axis Z_2 e.g., O_2. The location of origin points O_h and O_2 is specified by the position vectors $\boldsymbol{\rho}^{(1)}$

and $\boldsymbol{\rho}^{(2)}$, which are measured from the fixed coordinate system $S_f(X_f, Y_f, Z_f)$. **D** is a relative-position vector drawn from the point O_2 to point O_h.

According to section 3.3, the relative velocity with respect to the hob cutter surface Σ_1, $\mathbf{V}_r^{(1)}$, and relative velocity of the tip of the surface unit normal which corresponds to the motion of the contact point over the surface Σ_1, $\dot{\mathbf{n}}_r^{(i)}$, can be expressed by:

$$\begin{aligned}&\dot{\mathbf{n}}_r^{(i)} \cdot \mathbf{V}^{(12,j)} - \mathbf{V}_r^{(1)} \cdot (\boldsymbol{\omega}^{(12,j)} \times \mathbf{n}^{(i)}) + \mathbf{V}^{(12,j)} \cdot (\boldsymbol{\omega}^{(i)} \times \mathbf{n}^{(i)}) - \mathbf{P}^{(1)} \cdot (\dot{\boldsymbol{\omega}}^{(12,j)} \times \mathbf{n}^{(i)}) \\ &- (\boldsymbol{\omega}^{(1)} \times \mathbf{P}^{(1)}) \cdot (\boldsymbol{\omega}^{(12,j)} \times \mathbf{n}^{(i)}) + (\boldsymbol{\rho}^{(1)} - \boldsymbol{\rho}^{(2)}) \cdot (\dot{\boldsymbol{\omega}}^{(2,j)} \times \mathbf{n}^{(i)}) \\ &+ (\mathbf{V}^{(O_h)} - \mathbf{V}^{(O_2)}) \cdot (\boldsymbol{\omega}^{(2,j)} \times \mathbf{n}^{(i)}) + (\dot{\mathbf{V}}^{(O_h,j)} - \dot{\mathbf{V}}^{(O_2,j)}) \cdot \mathbf{n}^{(i)} = 0 .\end{aligned} \tag{4.6}$$

4.3 Relations Between Curvatures of Mating Surfaces

Figure 4.2 shows that two mating surfaces Σ_1 and Σ_2 are tangent to each other at their instantaneous contact point *M*. The vector $\mathbf{n}$ represents the surfaces common unit normal at common contact point *M*. Plane T denotes the common tangent plane of these two mating surfaces. The origins of coordinate systems $S_1(\mathbf{e}_f, \mathbf{e}_h, \mathbf{n})$, and $S_2(\mathbf{e}_s, \mathbf{e}_q, \mathbf{n})$, and the instantaneous contact point *M* are coincident. $\mathbf{e}_f$ and $\mathbf{e}_h$ are unit vectors of the principal directions of surface Σ_1, while $\mathbf{e}_s$ and $\mathbf{e}_q$ are unit vectors of the principal directions of surface Σ_2. σ is the angle measured from the vector $\mathbf{e}_f$ to $\mathbf{e}_s$. The coordinate transformation matrix, $\mathbf{L}_{21}$, and $\mathbf{L}_{12}$ transform the coordinates from coordinate system $S_1(\mathbf{e}_f, \mathbf{e}_h)$ to $S_2(\mathbf{e}_s, \mathbf{e}_q)$ and from $S_2(\mathbf{e}_s, \mathbf{e}_q)$ to $S_1(\mathbf{e}_f, \mathbf{e}_h)$, respectively, can be expressed by:

$$\mathbf{L}_{12} = \begin{bmatrix} \cos\sigma & -\sin\sigma \\ \sin\sigma & \cos\sigma \end{bmatrix}, \tag{4.7}$$

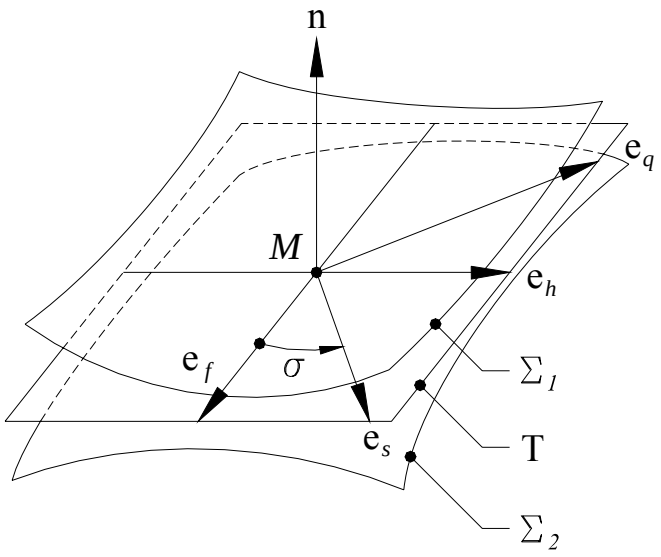

Fig. 4.2 Principal direction of mating surface represented in tangent plane

and $\mathbf{L}_{21} = \begin{bmatrix} \cos\sigma & \sin\sigma \\ -\sin\sigma & \cos\sigma \end{bmatrix}$. (4.8)

The vectors $\overset{\bullet}{\mathbf{n}}_r^{(i)}$ and $\mathbf{V}_r^{(i)}$ lie in the tangent plane T and they are related by Rodrigues' formula [12,13] as follows:

$$\begin{bmatrix} \overset{\bullet}{n}_f^{(1)} & \overset{\bullet}{n}_h^{(1)} \end{bmatrix}^T = \mathbf{K}_1 \begin{bmatrix} v_f^{(1)} & v_h^{(1)} \end{bmatrix}^T, \tag{4.9}$$

and $$\begin{bmatrix} \overset{\bullet}{n}_s^{(2)} & \overset{\bullet}{n}_q^{(2)} \end{bmatrix}^T = \mathbf{K}_2 \begin{bmatrix} v_s^{(2)} & v_q^{(2)} \end{bmatrix}^T, \tag{4.10}$$

where $\mathbf{K}_1 = \begin{bmatrix} -k_f & 0 \\ 0 & -k_h \end{bmatrix}$, and $\mathbf{K}_2 = \begin{bmatrix} -k_s & 0 \\ 0 & -k_q \end{bmatrix}$.

Symbols k_f and k_h are the principal curvatures of surface Σ_1, while k_s and k_q are the principal curvatures of surface Σ_2. Owing to the tangency of two contacting

surfaces, the position vectors of the surface Σ_1 and surface Σ_2 at the contact point and their unit normal vectors are the same as represented in the fixed coordinate system by:

$$\mathbf{R}^{(1)} = \mathbf{R}^{(2)}, \tag{4.11}$$

and $\mathbf{n}^{(1)} = \mathbf{n}^{(2)}$. (4.12)

The differentiated forms of Eqs. (4.11) and (4.12) can be represented as follows [12,13]:

$$\mathbf{V}_r^{(2)} = \mathbf{V}_r^{(1)} + \mathbf{V}_{tr}^{(12)}, \tag{4.13}$$

and $\dot{\mathbf{n}}_r^{(2)} = \dot{\mathbf{n}}_r^{(1)} + \boldsymbol{\omega}^{(12)} \times \mathbf{n}^{(1)}$. (4.14)

The subscript "r" represents the relative velocity over the tooth surface, while the subscript "tr" denotes the transfer velocity. Equations (4.13) and (4.14) can be rewritten in matrix form and represented in coordinate system $S_1(\mathbf{e}_f, \mathbf{e}_h)$ as follows:

$$\begin{bmatrix} v_f^{(2)} \\ v_h^{(2)} \end{bmatrix}_r = \begin{bmatrix} v_f^{(1)} \\ v_h^{(1)} \end{bmatrix}_r + \begin{bmatrix} v_f^{(12)} \\ v_h^{(12)} \end{bmatrix}_{tr}, \tag{4.15}$$

and $\begin{bmatrix} \dot{n}_f^{(2)} \\ \dot{n}_h^{(2)} \end{bmatrix}_r = \begin{bmatrix} \dot{n}_f^{(1)} \\ \dot{n}_h^{(1)} \end{bmatrix}_r + \begin{bmatrix} (\boldsymbol{\omega}^{(12)} \times \mathbf{n}^{(1)}) \cdot \mathbf{e}_f \\ (\boldsymbol{\omega}^{(12)} \times \mathbf{n}^{(1)}) \cdot \mathbf{e}_h \end{bmatrix}_{tr}$. (4.16)

Substituting Eqs. (4.9) ,(4.10) and (4.15) into Eq. (4.16) yields the following equation:

$$\{\mathbf{K}_1 - \mathbf{L}_{12}\mathbf{K}_2\mathbf{L}_{21}\} \begin{bmatrix} v_f^{(2)} \\ v_h^{(2)} \end{bmatrix}_r = \mathbf{K}_1 \begin{bmatrix} v_f^{(12)} \\ v_h^{(12)} \end{bmatrix}_{tr} + \begin{bmatrix} (\mathbf{n}^{(1)} \times \boldsymbol{\omega}^{(12)}) \cdot \mathbf{e}_f \\ (\mathbf{n}^{(1)} \times \boldsymbol{\omega}^{(12)}) \cdot \mathbf{e}_h \end{bmatrix}_{tr}. \tag{4.17}$$

After some mathematical operations, equation (4.17) can be represented by a system of two linear equations as follows:

$$\begin{bmatrix} b_{11} & b_{12} \\ b_{21} & b_{22} \end{bmatrix} \begin{bmatrix} v_f^{(2)} \\ v_h^{(2)} \end{bmatrix}_r + \begin{bmatrix} b_{13} & b_{14} \\ b_{23} & b_{24} \end{bmatrix} \begin{bmatrix} \dfrac{d\theta}{dt} \\ \dfrac{d\psi}{dt} \end{bmatrix} = 0 . \tag{4.18}$$

where $\begin{bmatrix} b_{11} & b_{12} \\ b_{21} & b_{22} \end{bmatrix} = \mathbf{K}_1 - \mathbf{L}_{12}\mathbf{K}_2\mathbf{L}_{21}$, (4.19)

$$\begin{bmatrix} b_{13} & b_{14} \\ b_{23} & b_{24} \end{bmatrix} \begin{bmatrix} \dfrac{d\theta}{dt} \\ \dfrac{d\psi}{dt} \end{bmatrix} = -\mathbf{K}_1 \begin{bmatrix} v_f^{(12)} \\ v_h^{(12)} \end{bmatrix}_{tr} - \begin{bmatrix} (\mathbf{n}^{(1)} \times \boldsymbol{\omega}^{(12)}) \cdot \mathbf{e}_f \\ (\mathbf{n}^{(1)} \times \boldsymbol{\omega}^{(12)}) \cdot \mathbf{e}_h \end{bmatrix}_{tr} , \tag{4.20}$$

$$b_{11} = -k_f + k_s \cos^2\sigma + k_q \sin^2\sigma = -k_f + 0.5(k_s + k_q) + 0.5(k_s - k_q)\cos 2\sigma , \tag{4.21}$$

$$b_{12} = b_{21} = -(k_q - k_s)\cos\sigma \sin\sigma = 0.5(k_s - k_q)\sin 2\sigma , \tag{4.22}$$

and $b_{22} = -k_h + k_q \cos^2\sigma + k_s \sin^2\sigma = -k_h + 0.5(k_s + k_q) - (k_s - k_q)\cos 2\sigma$. (4.23)

Equations (4.21)-(4.23) yield:

$$\tan 2\sigma = \frac{2b_{12}}{b_{11} - b_{22} + k_f - k_h} , \tag{4.24}$$

$$k_s = \frac{1}{2}(b_{11} + b_{22} + k_f + k_h + \frac{2b_{12}}{\sin 2\sigma}) , \tag{4.25}$$

and $k_q = \frac{1}{2}(b_{11} + b_{22} + k_f + k_h - \frac{2b_{12}}{\sin 2\sigma})$. (4.26)

Let $i = 1$ and j=θ in Eq. (4.6) and substituting Eqs. (4.9) and (4.15) into Eq. (4.6), equation (4.6) can be expressed by:

$$\begin{bmatrix} b_{31} & b_{32} \end{bmatrix} \begin{bmatrix} v_f^{(2)} \\ v_h^{(2)} \end{bmatrix}_r + \begin{bmatrix} b_{33} & b_{34} \end{bmatrix} \begin{bmatrix} \dfrac{d\theta}{dt} \\ \dfrac{d\psi}{dt} \end{bmatrix} = 0 , \tag{4.27}$$

where $\begin{bmatrix} b_{31} \\ b_{32} \end{bmatrix}^T = \begin{bmatrix} v_f^{(12,\theta)} \\ v_h^{(12,\theta)} \end{bmatrix}^T \mathbf{K}_1 + \begin{bmatrix} (\mathbf{n}^{(1)} \times \boldsymbol{\omega}^{(12,\theta)}) \cdot \mathbf{e}_f \\ (\mathbf{n}^{(1)} \times \boldsymbol{\omega}^{(12,\theta)}) \cdot \mathbf{e}_h \end{bmatrix}^T$, (4.28)

$$\begin{bmatrix} b_{33} & b_{34} \end{bmatrix} \begin{bmatrix} \dfrac{d\theta}{dt} \\ \dfrac{d\psi}{dt} \end{bmatrix} = k_f v_f^{(12,\theta)} v_f^{(12)} + k_h v_h^{(12,\theta)} v_h^{(12)} - [\mathbf{n}^{(1)} \boldsymbol{\omega}^{(12,\theta)} \mathbf{V}_{tr}^{(12)}] + [\mathbf{V}^{(12,\theta)} \boldsymbol{\omega}^{(1)} \mathbf{n}^{(1)}]$$

and
$$-[\mathbf{P}^{(1)} \dot{\boldsymbol{\omega}}^{(12,\theta)} \mathbf{n}^{(1)}] - [(\boldsymbol{\omega}^{(1)} \times \mathbf{P}^{(1)}) \boldsymbol{\omega}^{(12,\theta)} \mathbf{n}^{(1)}] + [(\boldsymbol{\rho}^{(1)} - \boldsymbol{\rho}^{(2)}) \dot{\boldsymbol{\omega}}^{(2,\theta)} \mathbf{n}^{(1)}] .$$
$$+ [(\mathbf{V}^{(O_h)} - \mathbf{V}^{(O_2)}) \boldsymbol{\omega}^{(2,\theta)} \mathbf{n}^{(1)}] + (\dot{\mathbf{V}}^{(O_h,\theta)} - \dot{\mathbf{V}}^{(O_2,\theta)}) \cdot \mathbf{n}^{(1)}$$

(4.29)

Similarly, setting $i = 1$ and j $= \psi$ in Eq. (4.6) and substituting Eqs. (4.9) and (4.15) into Eq. (4.6), equation (4.6) can be expressed by:

$$\begin{bmatrix} b_{41} & b_{42} \end{bmatrix} \begin{bmatrix} v_f^{(2)} \\ v_h^{(2)} \end{bmatrix}_r + \begin{bmatrix} b_{43} & b_{44} \end{bmatrix} \begin{bmatrix} \dfrac{d\theta}{dt} \\ \dfrac{d\psi}{dt} \end{bmatrix} = 0 , \tag{4.30}$$

where $$\begin{bmatrix} b_{41} \\ b_{42} \end{bmatrix}^T = \begin{bmatrix} v_f^{(12,\psi)} \\ v_h^{(12,\psi)} \end{bmatrix}^T \mathbf{K}_1 + \begin{bmatrix} (\mathbf{n}^{(1)} \times \boldsymbol{\omega}^{(12,\psi)}) \cdot \mathbf{e}_f \\ (\mathbf{n}^{(1)} \times \boldsymbol{\omega}^{(12,\psi)}) \cdot \mathbf{e}_h \end{bmatrix}^T , \tag{4.31}$$

$$\begin{bmatrix} b_{43} & b_{44} \end{bmatrix} \begin{bmatrix} \dfrac{d\theta}{dt} \\ \dfrac{d\psi}{dt} \end{bmatrix} = k_f v_f^{(12,\psi)} v_f^{(12)} + k_h v_h^{(12,\psi)} v_h^{(12)} - [\mathbf{n}^{(1)} \boldsymbol{\omega}^{(12,\psi)} \mathbf{V}_{tr}^{(12)}] + [\mathbf{V}^{(12,\psi)} \boldsymbol{\omega}^{(1)} \mathbf{n}^{(1)}]$$

and
$$-[\mathbf{P}^{(1)} \dot{\boldsymbol{\omega}}^{(12,\psi)} \mathbf{n}^{(1)}] - [(\boldsymbol{\omega}^{(1)} \times \mathbf{P}^{(1)}) \boldsymbol{\omega}^{(12,\psi)} \mathbf{n}^{(1)}] + [(\boldsymbol{\rho}^{(1)} - \boldsymbol{\rho}^{(2)}) \dot{\boldsymbol{\omega}}^{(2,\psi)} \mathbf{n}^{(1)}] .$$
$$+ [(\mathbf{V}^{(O_h)} - \mathbf{V}^{(O_2)}) \boldsymbol{\omega}^{(2,\psi)} \mathbf{n}^{(1)}] + (\dot{\mathbf{V}}^{(O_h,\psi)} - \dot{\mathbf{V}}^{(O_2,\psi)}) \cdot \mathbf{n}^{(1)}$$

(4.32)

Equations (4.18), (4.27), and (4.30) yield a system of four equations in two unknowns as follows:

$$\begin{bmatrix} b_{11} & b_{12} & b_{13} & b_{14} \\ b_{21} & b_{22} & b_{23} & b_{24} \\ b_{31} & b_{32} & b_{33} & b_{34} \\ b_{41} & b_{42} & b_{43} & b_{44} \end{bmatrix} \begin{bmatrix} v_f^{(2)} \\ v_h^{(2)} \\ \dfrac{d\theta}{dt} \\ \dfrac{d\psi}{dt} \end{bmatrix} = 0 , \tag{4.33}$$

As shown in Fig 2.5, the curvilinear-tooth gears are generated by a CNC hobbing

machine. The kinematic relations such as position vectors $\mathbf{P}^{(i)}$ and $\boldsymbol{\rho}^{(i)}$, linear velocities $\mathbf{V}^{(O_h)}$ and $\mathbf{V}^{(O_2)}$, angular velocities $\boldsymbol{\omega}^{(1)}$ and $\boldsymbol{\omega}^{(2)}$, and their differentiation have been derived in section 3.2. Substituting these kinematic relations into Eqs. (4.18), (4.27), and (4.30), the coefficients of the system of four equations (4.33) can be found.

Since the velocity of the contact point in its motion over the surface has unique direction, the system of linear equation (4.33) must possess a unique solution. Thus the rank of matrix of coefficients for equation (4.33) must equal to two. This yields:

$$\begin{vmatrix} b_{11} & b_{13} & b_{14} \\ b_{31} & b_{33} & b_{34} \\ b_{41} & b_{43} & b_{44} \end{vmatrix} = 0, \tag{4.34}$$

$$\begin{vmatrix} b_{22} & b_{23} & b_{24} \\ b_{32} & b_{33} & b_{34} \\ b_{42} & b_{43} & b_{44} \end{vmatrix} = 0, \tag{4.35}$$

$$\begin{vmatrix} b_{12} & b_{13} & b_{14} \\ b_{32} & b_{33} & b_{34} \\ b_{42} & b_{43} & b_{44} \end{vmatrix} = 0. \tag{4.36}$$

According to Eqs. (4.34)-(4.36), the coefficients b_{11}, b_{12}, and b_{22}, can be obtained as follows:

$$b_{11} = \frac{b_{13}b_{34}b_{41} + b_{14}b_{43}b_{31} - b_{14}b_{33}b_{41} - b_{13}b_{31}b_{44}}{b_{33}b_{44} - b_{34}b_{43}}, \tag{4.37}$$

$$b_{12} = \frac{b_{13}b_{34}b_{42} + b_{14}b_{43}b_{32} - b_{14}b_{33}b_{42} - b_{13}b_{32}b_{44}}{b_{33}b_{44} - b_{34}b_{43}}, \tag{4.38}$$

$$b_{22} = \frac{b_{23}b_{34}b_{42} + b_{24}b_{43}b_{32} - b_{24}b_{33}b_{42} - b_{23}b_{32}b_{44}}{b_{33}b_{44} - b_{34}b_{43}}, \tag{4.39}$$

Substituting the coefficients b_{11}, b_{12}, and b_{22}, and the principal curvatures k_f and k_h of the tool surface into Eqs. (4.24)-(4.26), the unknown principal curvatures

k_s and k_q of the generated surface and the angle σ formed between the vectors $\mathbf{e}_f$ and $\mathbf{e}_s$ can be found.

4.4 Principal Curvatures and Directions of the Hob Cutter

The tooth surfaces of cylindrical gears with curvilinear shaped teeth generated by a hob cutter that is performing motion with two independent parameters had been developed in chapter 2. The surface equation of the hob cutter $\mathbf{r}_1^{(1)}$, represented in coordinate system $S_1(X_1, Y_1, Z_1)$, can be expressed by:

$$\mathbf{r}_1^{(1)}(l_1, \phi_1) = \begin{bmatrix} (r_t + l_1 \cos\alpha_n)\cos\phi_1 \mp l_1 \sin\alpha_n \sin\phi_1 \sin\beta \\ -(r_t + l_1 \cos\alpha_n)\sin\phi_1 \mp l_1 \sin\alpha_n \cos\phi_1 \sin\beta \\ \pm l_1 \sin\alpha_n \cos\beta - P_1\phi_1 \\ 1 \end{bmatrix}, \tag{4.40}$$

where l_1 and ϕ_1 are the surface parameters of the hob cutter. P_1 denotes the lead-per-radian revolution of the hob cutter's surface. Symbols α_n, β, and r_t are design parameters of the hob cutter. In Eq. (4.40), the upper sign represents the right-side hob cutter surface while the lower sign indicates the left-side hob cutter surface.

The surface normal vector $\mathbf{N}_1^{(1)}$ of the hob cutter can be obtained and represented in coordinate system $S_1(X_1, Y_1, Z_1)$ as follows:

$$\mathbf{N}_1^{(1)} = \mathbf{r}_l \times \mathbf{r}_\phi, \tag{4.41}$$

where $\mathbf{r}_l = \dfrac{\partial \mathbf{r}_1^{(1)}}{\partial l_1} = \begin{bmatrix} \cos\alpha_n \cos\phi_1 \mp \sin\alpha_n \sin\phi_1 \sin\beta \\ -\cos\alpha_n \sin\phi_1 \mp \sin\alpha_n \cos\phi_1 \sin\beta \\ \pm \sin\alpha_n \cos\beta \end{bmatrix}$,

and $\mathbf{r}_\phi = \dfrac{\partial \mathbf{r}_1^{(1)}}{\partial \phi_1} = \begin{bmatrix} -(r_t + l_1 \cos\alpha_n)\sin\phi_1 \mp l_1 \sin\alpha_n \cos\phi_1 \sin\beta \\ -(r_t + l_1 \cos\alpha_n)\cos\phi_1 \pm l_1 \sin\alpha_n \sin\phi_1 \sin\beta \\ -P_1 \end{bmatrix}$.

The principal curvatures k_f and k_h, and principal directions $\mathbf{e}_f$ and $\mathbf{e}_h$ of the point on surface can be expressed by [56]:

$$k_f = H + \sqrt{H^2 - K}\,, \tag{4.42}$$

$$k_h = H - \sqrt{H^2 - K}\,, \tag{4.43}$$

$$\mathbf{e}_f = (\mathbf{r}_l \frac{dl}{d\phi} + \mathbf{r}_\phi) \Big/ \left| \mathbf{r}_l \frac{dl}{d\phi} + \mathbf{r}_\phi \right| \quad , \frac{dl}{d\phi} = \frac{-(k_f F - M)}{k_f E - L}, \tag{4.44}$$

$$\mathbf{e}_h = (\mathbf{r}_l \frac{dl}{d\phi} + \mathbf{r}_\phi) \Big/ \left| \mathbf{r}_l \frac{dl}{d\phi} + \mathbf{r}_\phi \right| \quad , \frac{dl}{d\phi} = \frac{-(k_h F - M)}{k_h E - L}, \tag{4.45}$$

where $H = \dfrac{k_f + k_h}{2} = \dfrac{EN - 2FM + GL}{2(EG - F^2)}$, $K = k_f k_h = \dfrac{LN - M^2}{EG - F^2}$,

$E = \mathbf{r}_l \cdot \mathbf{r}_l$, $F = \mathbf{r}_l \cdot \mathbf{r}_\phi$, $G = \mathbf{r}_\phi \cdot \mathbf{r}_\phi$, $L = \mathbf{r}_{ll} \cdot \mathbf{n}^{(1)}$, $M = \mathbf{r}_{l\phi} \cdot \mathbf{n}^{(1)}$

and $N = \mathbf{r}_{\phi\phi} \cdot \mathbf{n}^{(1)}$.

Symbol H represents the mean curvature while K expresses the Gaussian curvature. The partial derivatives $\mathbf{r}_{ll}$, $\mathbf{r}_{l\phi}$, and $\mathbf{r}_{\phi\phi}$ of surface equation $\mathbf{r}_1^{(1)}$, represented in coordinate system $S_1(X_1, Y_1, Z_1)$, can be obtained by:

$$\mathbf{r}_{ll} = 0, \tag{4.46}$$

$$\mathbf{r}_{l\phi} = \mathbf{r}_{\phi l} = \begin{bmatrix} -\cos\alpha_n \sin\phi_1 \mp \sin\alpha_n \cos\phi_1 \sin\beta \\ -\cos\alpha_n \cos\phi_1 \pm \sin\alpha_n \sin\phi_1 \sin\beta \\ 0 \end{bmatrix}, \tag{4.47}$$

$$\mathbf{r}_{\phi\phi} = \begin{bmatrix} -(r_t + l_1 \cos\alpha_n)\cos\phi_1 \pm l_1 \sin\alpha_n \sin\phi_1 \sin\beta \\ (r_t + l_1 \cos\alpha_n)\sin\phi_1 \pm l_1 \sin\alpha_n \cos\phi_1 \sin\beta \\ 0 \end{bmatrix}. \tag{4.48}$$

Substituting the partial derivatives $\mathbf{r}_l$, $\mathbf{r}_\phi$, $\mathbf{r}_{l\phi}$, and $\mathbf{r}_{\phi\phi}$ into Eqs. (4.42)-(4.45), the principal curvatures and directions of a point on hob cutter surface can be obtained.

4.5 Numerical Examples

The procedures for determination of principal curvatures and directions of a two-parameter envelope surface are shown in Fig. 4.3. There are two numerical examples to calculate the principal curvatures and directions at the point of tooth surface of the curvilinear-tooth gear.

Example 4.1: The major design parameters of a ZA worm-type hob cutter and the curvilinear-tooth gear are listed in Table 4.1. Figure 4.4 displays the left-side and right-side tooth surfaces of the curvilinear-tooth gear, Σ_{2L} and Σ_{2R}. The cross section Z_f=0.0 mm shown in Fig. 4.4 represents the middle section of the tooth width.

Based on the flowchart shown in Fig. 4.3 and the corresponding equations, the principal curvatures and directions of the curvilinear-tooth gear surface can be obtained. When the nominal radius of circular arc tooth trace R_c equals 110 mm, Table 4.2 and Table 4.3 show the principal curvatures, k_s and k_q, and principal directions, $\mathbf{e}_s$ and $\mathbf{e}_q$, at cross section Z_f=0.0 mm on the tooth surfaces Σ_{2L} and Σ_{2R}, respectively. In Tables 4.2 and 4.3, l_1=4.381 mm generates the tip of addendum while l_1=10.354 mm generates the starting point of the working curve on the tooth surface.

According to the data of e_{sx}, e_{sy}, e_{sz}, e_{qx}, e_{qy}, and e_{qz} shown in Tables 4.2 and 4.3, it was found that the principal direction $\mathbf{e}_s$ is parallel to axis Z_f and the principal direction $\mathbf{e}_q$ lies in the plane $X_f - Y_f$. Since the principal curvatures k_s is positive and k_q is negative as shown in Table 4.2, the points at cross section

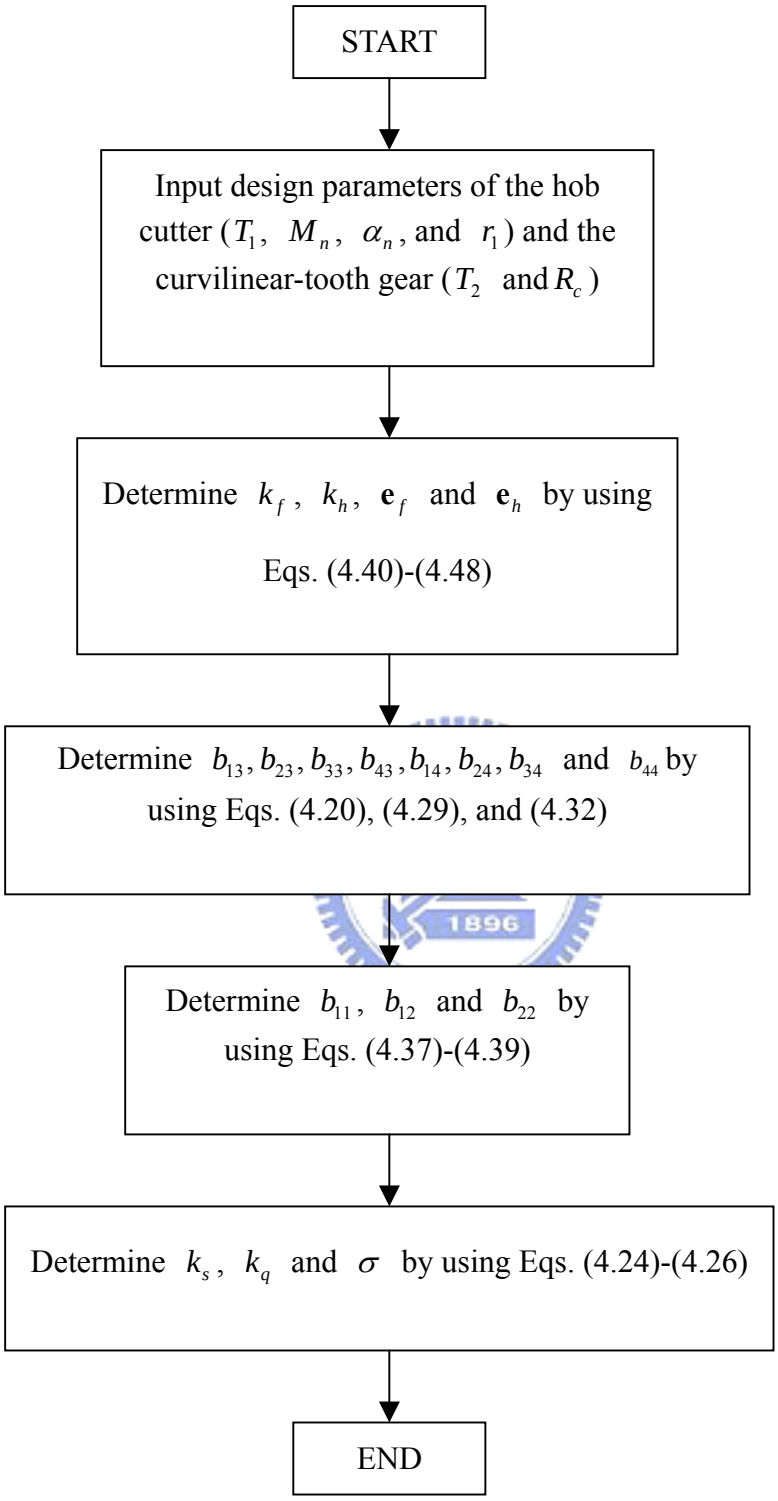

Fig. 4.3 Flowchart for the determination of the principal curvatures and directions for the envelope surface of family of tool surface

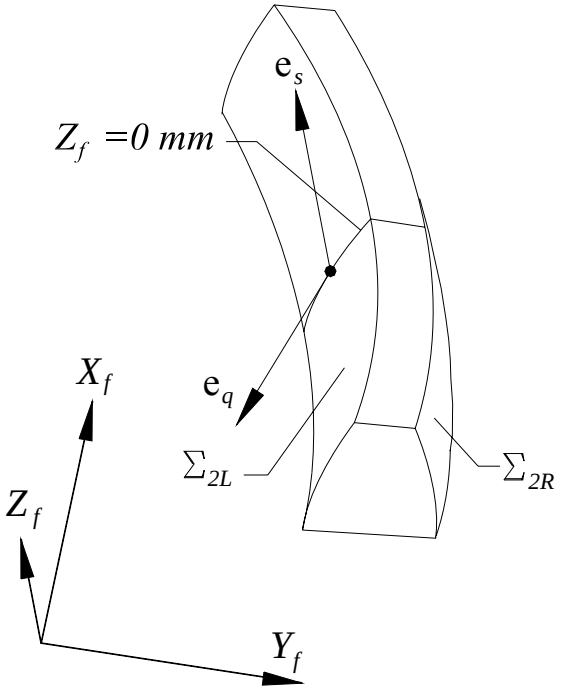

Fig. 4.4 The concave surface and convex surface of the curvilinear-tooth gear

Table 4.1 Major design parameters for cylindrical gears with circular arc tooth traces

	Hob cutter	Curvilinear-tooth gear
Number of teeth	1	20
Normal module	3 mm	3 mm
Normal pressure angle	20°	20°
Lead angle	2.866°	—
Face width	—	40 mm
Nominal radius of circular tooth trace	—	110 mm
Pitch radius	30 mm	30 mm
Outside diameter	67.5 mm	66 mm

Z_f = 0 mm on tooth surface Σ_{2L} are hyperbolic points. The points at cross section Z_f = 0 mm on tooth surface Σ_{2R} are elliptic points because the principal curvatures k_s and k_q both have the same sign as shown in Table 4.3.

Example 4.2: The major design parameters are chosen the same as those shown in Table 4.1, except that the nominal radius of circular arc tooth trace R_c is 5000 mm. The analysis results of principal curvatures and directions are shown in Table 4.4 and Table 4.5. It is found that the characteristics of curvatures and directions of the surfaces are the same as those shown in Table 4.2 and Table 4.3, except that the principal curvatures k_s of the points at cross section Z_f = 0 mm have some differences.

Table 4.2 Principal curvatures and directions at cross section Z_f = 0 mm on tooth surface Σ_{2L} when nominal radius R_c = 110 mm

l_1 (mm)	k_s (1/mm)	e_{sx}	e_{sy}	e_{sz}	k_q (1/mm)	e_{qx}	e_{qy}	e_{qz}
4.381	0.009077	0.000	0.000	1.000	-0.058372	-0.870	-0.493	0.000
4.979	0.008944	0.000	0.000	1.000	-0.064565	-0.897	-0.441	0.000
5.576	0.008815	0.000	0.000	1.000	-0.072231	-0.922	-0.388	0.000
6.173	0.008690	0.000	0.000	1.000	-0.081965	-0.943	-0.334	0.000
6.770	0.008568	0.000	0.000	1.000	-0.094734	-0.961	-0.278	0.000
7.368	0.008449	0.000	0.000	1.000	-0.112222	-0.975	-0.222	0.000
7.965	0.008334	0.000	0.000	1.000	-0.137634	-0.986	-0.164	0.000
8.562	0.008221	0.000	0.000	1.000	-0.177932	-0.994	-0.106	0.000
9.159	0.008112	0.000	0.000	1.000	-0.251613	-0.999	-0.048	0.000
9.757	0.008006	0.000	0.000	1.000	-0.429482	-1.000	0.010	0.000
10.354	0.007902	0.000	0.000	1.000	-1.465754	-0.998	0.068	0.000

Table 4.3 Principal curvatures and directions at cross section Z_f = 0 mm on tooth surface Σ_{2R} when nominal radius R_c = 110 mm

l_1 (mm)	k_s (1/mm)	e_{sx}	e_{sy}	e_{sz}	k_q (1/mm)	e_{qx}	e_{qy}	e_{qz}
4.381	0.008067	0.000	0.000	1.000	0.058372	0.870	-0.493	0.000
4.979	0.008176	0.000	0.000	1.000	0.064565	0.897	-0.441	0.000
5.576	0.008287	0.000	0.000	1.000	0.072231	0.922	-0.388	0.000
6.173	0.008402	0.000	0.000	1.000	0.081965	0.943	-0.334	0.000
6.770	0.008520	0.000	0.000	1.000	0.094734	0.961	-0.278	0.000
7.368	0.008641	0.000	0.000	1.000	0.112222	0.975	-0.222	0.000
7.965	0.008766	0.000	0.000	1.000	0.137634	0.986	-0.164	0.000
8.562	0.008895	0.000	0.000	1.000	0.177932	0.994	-0.106	0.000
9.159	0.009027	0.000	0.000	1.000	0.251613	0.999	-0.048	0.000
9.757	0.009163	0.000	0.000	1.000	0.429482	1.000	0.010	0.000
10.354	0.009304	0.000	0.000	1.000	1.465754	0.998	0.068	0.000

Table 4.4 Principal curvatures and directions at cross section Z_f = 0 mm on tooth surface Σ_{2L} when nominal radius R_c = 5000 mm

l_1 (mm)	k_s (1/mm)	e_{sx}	e_{sy}	e_{sz}	k_q (1/mm)	e_{qx}	e_{qy}	e_{qz}
4.381	1.881729E-4	0.000	0.000	1.000	-0.058372	-0.870	-0.493	0.000
4.979	1.881244E-4	0.000	0.000	1.000	-0.064565	-0.897	-0.441	0.000
5.576	1.880755E-4	0.000	0.000	1.000	-0.072231	-0.922	-0.388	0.000
6.173	1.880260E-4	0.000	0.000	1.000	-0.081965	-0.943	-0.334	0.000
6.770	1.879760E-4	0.000	0.000	1.000	-0.094734	-0.961	-0.278	0.000
7.368	1.879256E-4	0.000	0.000	1.000	-0.112222	-0.975	-0.222	0.000
7.965	1.878748E-4	0.000	0.000	1.000	-0.137634	-0.986	-0.164	0.000
8.562	1.878236E-4	0.000	0.000	1.000	-0.177932	-0.994	-0.106	0.000
9.159	1.877721E-4	0.000	0.000	1.000	-0.251613	-0.999	-0.048	0.000
9.757	1.877203E-4	0.000	0.000	1.000	-0.429482	-1.000	0.010	0.000
10.354	1.876682E-4	0.000	0.000	1.000	-1.465754	-0.998	0.068	0.000

Table 4.5 Principal curvatures and directions at cross section Z_f = 0 mm on tooth surface Σ_{2R} when nominal radius R_c = 5000 mm

l_1 (mm)	k_s (1/mm)	e_{sx}	e_{sy}	e_{sz}	k_q (1/mm)	e_{qx}	e_{qy}	e_{qz}
4.381	1.876860E-4	0.000	0.000	1.000	0.058372	0.870	-0.493	0.000
4.979	1.877534E-4	0.000	0.000	1.000	0.064565	0.897	-0.441	0.000
5.576	1.878204E-4	0.000	0.000	1.000	0.072231	0.922	-0.388	0.000
6.173	1.878869E-4	0.000	0.000	1.000	0.081965	0.943	-0.334	0.000
6.770	1.879529E-4	0.000	0.000	1.000	0.094734	0.961	-0.278	0.000
7.368	1.880186E-4	0.000	0.000	1.000	0.112222	0.975	-0.222	0.000
7.965	1.880840E-4	0.000	0.000	1.000	0.137634	0.986	-0.164	0.000
8.562	1.881490E-4	0.000	0.000	1.000	0.177932	0.994	-0.106	0.000
9.159	1.882137E-4	0.000	0.000	1.000	0.251613	0.999	-0.048	0.000
9.757	1.882782E-4	0.000	0.000	1.000	0.429482	1.000	0.010	0.000
10.354	1.883423E-4	0.000	0.000	1.000	1.465754	0.998	0.068	0.000

4.6 Remarks

An approach for the determination of principal curvatures and directions for the surface as envelope to two parameters family of surfaces has been developed. The proposed approach has considered three equations, two differentiated equations of meshing and Rodrigues' equation, to yield system of four linear equations in two unknowns. It was the extension of Litvin's approach.

Computer programs for calculations of the principal curvatures and directions of the tooth surfaces have been developed. The principal curvatures and directions of the tooth surface have been calculated successfully by the developed computer programs. The proposed approach will be further used to evaluate the half length of the major and minor axes of contact ellipse in the next chapter.

CHAPTER 5

Tooth Contact Anaylsis

5.1 Introduction

The noise and vibration of gear meshing are two important measurements of a gear train performance. It is well known that the kinematic error (KE) of a gear train is a main source of gear noise and vibration [55]. The shape and level of KEs induced by gear axial misalignments are the important factors to predict the noise and vibration of a mating gear pair. If the KE is a discontinuous function, there has a relative motion and a large acceleration at the transfer point where the next gear pair come into mesh. The shape of KEs with discontinuous linear function caused by gear axial-misalignments can be absorbed by a predesigned parabolic function of KEs with a controllable magnitude [13], and the level of KEs induced by horizontal axial-misalignments can be reduced by the compensation method [25]. The bearing contact may be shifted to the edge of the gear tooth surfaces due to the errors of manufacturing or assembly. To avoid the edge contact of a mating gear pair, the tooth surfaces should be modified to change the contact type from line contact to point contact. Gear pairs with higher contact ratios can reduce the tooth stress and KE by sharing the load among neighboring teeth. The dimensions and orientation of contact ellipses can be obtained and the finite element method is applied to the stress analysis.

The contact characteristics of the gear pair mentioned above, the paths of the contact point on tooth surfaces as well as contact ratio, KE, and contact ellipse can be estimated by the developed tooth contact analysis (TCA) computer program. Assumptions, such as considering contact as rigid surfaces, have been made when the

tooth contact analysis is performed. In this chapter, the contact characteristics of a curvilinear-tooth gear pair will be studied.

5.2 Simulation of Gear Meshing

The model for gear meshing under assembly errors can be simulated by changing the settings and orientations of the coordinate systems $S_h(X_h, Y_h, Z_h)$ and $S_v(X_v, Y_v, Z_v)$ with respect to the fixed coordinate system S_f as shown in Fig. 5.1, where coordinate systems $S_p(X_p, Y_p, Z_p)$ and $S_g(X_g, Y_g, Z_g)$ are attached to the pinion and gear, respectively. The axes Z_p and Z_g are rotational axes of the pinion and gear, respectively. Coordinate systems $S_v(X_v, Y_v, Z_v)$ and $S_h(X_h, Y_h, Z_h)$ are the reference coordinate systems for the misaligned gear assembly simulations. The simulation of horizontal axial misalignments of a gear pair can be achieved by rotating the coordinate system $S_h(X_h, Y_h, Z_h)$ about the X_h axis through an angle $\Delta\gamma_h$ with respect to the coordinate system $S_f(X_f, Y_f, Z_f)$. Similarly, simulation of vertical axial misalignments of a gear pair can be performed by rotating the coordinate system $S_v(X_v, Y_v, Z_v)$ about the Y_h through an angle $\Delta\gamma_v$ with respect to coordinate system $S_h(X_h, Y_h, Z_h)$. ΔZ denotes the assembly error along the rotational axis Z_g measured from point O_g' to point O_g. Symbol C' represents the operational center distance of a gear pair, and ΔC denotes the center distance variations. The origin O_g of the coordinate system $S_g(X_g, Y_g, Z_g)$ may be displaced by an amount of ΔC and the operational center distance of the meshing gear pair can be represented by $C' = C + \Delta C$ with respect to origin O_f of the fixed coordinate system $S_f(X_f, Y_f, Z_f)$. Symbols ϕ_1' and ϕ_2' represent the rotational

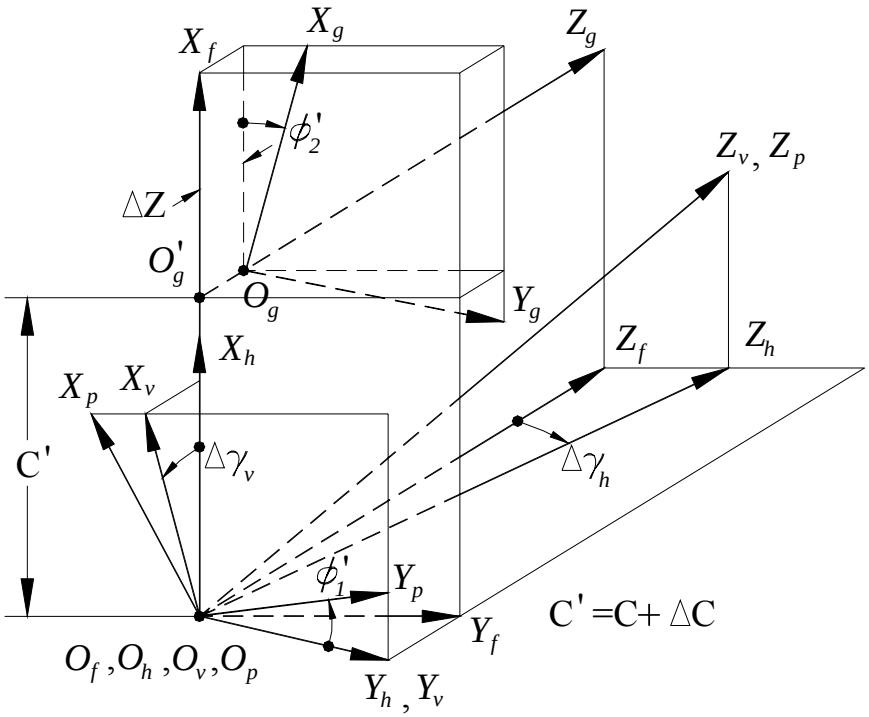

Fig. 5.1 Simulation of gear meshing with assembly errors

angles of the pinion and gear, respectively, when they are meshed with each other.

The unit normal and position vectors of both pinion and gear tooth surfaces should be represented in the same coordinate system, say $S_f(X_f, Y_f, Z_f)$ when applying the TCA method to calculate the KEs of the curvilinear gear pair. The position vector and the unit normal vector of the pinion represented in coordinate system $S_p(X_p, Y_p, Z_p)$ can be transformed to the fixed coordinate system $S_f(X_f, Y_f, Z_f)$ by applying the following homogeneous coordinate transformation

matrix equations:

$$\mathbf{R}_f^{(p)} = \mathbf{M}_{fh}\mathbf{M}_{hv}\mathbf{M}_{vp}\mathbf{R}_p^{(p)} \tag{5.1}$$

and $\mathbf{n}_f^{(p)} = \mathbf{L}_{fh}\mathbf{L}_{hv}\mathbf{L}_{vp}\mathbf{n}_p^{(p)}$ (5.2)

where $\mathbf{M}_{vp} = \begin{bmatrix} \cos\phi_1' & \sin\phi_1' & 0 & 0 \\ -\sin\phi_1' & \cos\phi_1' & 0 & 0 \\ 0 & 0 & 1 & 0 \\ 0 & 0 & 0 & 1 \end{bmatrix}$,

$$\mathbf{M}_{hv} = \begin{bmatrix} \cos\Delta\gamma_v & 0 & \sin\Delta\gamma_v & 0 \\ 0 & 1 & 0 & 0 \\ -\sin\Delta\gamma_v & 0 & \cos\Delta\gamma_v & 0 \\ 0 & 0 & 0 & 1 \end{bmatrix},$$

$$\mathbf{M}_{fh} = \begin{bmatrix} 1 & 0 & 0 & 0 \\ 0 & \cos\Delta\gamma_h & \sin\Delta\gamma_h & 0 \\ 0 & -\sin\Delta\gamma_h & \cos\Delta\gamma_h & 0 \\ 0 & 0 & 0 & 1 \end{bmatrix},$$

$$\mathbf{L}_{vp} = \begin{bmatrix} \cos\phi_1' & \sin\phi_1' & 0 \\ -\sin\phi_1' & \cos\phi_1' & 0 \\ 0 & 0 & 1 \end{bmatrix},$$

$$\mathbf{L}_{hv} = \begin{bmatrix} \cos\Delta\gamma_v & 0 & \sin\Delta\gamma_v \\ 0 & 1 & 0 \\ -\sin\Delta\gamma_v & 0 & \cos\Delta\gamma_v \end{bmatrix},$$

and $\mathbf{L}_{fh} = \begin{bmatrix} 1 & 0 & 0 \\ 0 & \cos\Delta\gamma_h & \sin\Delta\gamma_h \\ 0 & -\sin\Delta\gamma_h & \cos\Delta\gamma_h \end{bmatrix}$.

Similarly, the position vector and the unit normal vector of the gear represented in coordinate system $S_g(X_g, Y_g, Z_g)$ can be transformed to the fixed coordinate system $S_f(X_f, Y_f, Z_f)$ by applying the following equations:

$$\mathbf{R}_f^{(g)} = \mathbf{M}_{fg}\mathbf{R}_g^{(g)} \tag{5.3}$$

and $\mathbf{n}_f^{(g)} = \mathbf{L}_{fg}\mathbf{n}_g^{(g)}$ (5.4)

where $\mathbf{M}_{fg} = \begin{bmatrix} \cos\phi_2' & -\sin\phi_2' & 0 & C' \\ \sin\phi_2' & \cos\phi_2' & 0 & 0 \\ 0 & 0 & 1 & \Delta Z \\ 0 & 0 & 0 & 1 \end{bmatrix}$,

and $\mathbf{L}_{fg} = \begin{bmatrix} \cos\phi_2' & -\sin\phi_2' & 0 \\ \sin\phi_2' & \cos\phi_2' & 0 \\ 0 & 0 & 1 \end{bmatrix}$.

5.3 Kinematic Errors

Owing to the tangency of two contacting gear tooth surfaces, the position vectors of the pinion and gear tooth surfaces should be the same at the contact points and their unit normal vectors should be collinear to each other. Therefore, the following equations must be held [12,13]:

$$\mathbf{R}_f^{(p)} - \mathbf{R}_f^{(g)} = 0, \tag{5.5}$$

and $$\mathbf{n}_f^{(p)} - \mathbf{n}_f^{(g)} = 0, \tag{5.6}$$

where $\mathbf{R}_f^{(p)}$ and $\mathbf{R}_f^{(g)}$ indicate the position vectors of the tooth surfaces of pinion and gear, respectively, represented in coordinate system $S_f(X_f, Y_f, Z_f)$. $\mathbf{n}_f^{(p)}$ and $\mathbf{n}_f^{(g)}$ express the surface unit normal vectors of pinion and gear, respectively, represented in coordinate system $S_f(X_f, Y_f, Z_f)$. Eq. (5.5) indicates that the pinion and gear tooth surfaces have a common contact point, and Eq. (5.6) indicates that the unit normal vectors of the pinion and gear surfaces are collinear at their contact point. Since $\left|\mathbf{n}_f^{(p)}\right| = \left|\mathbf{n}_f^{(g)}\right| = 1$, Eqs. (5.5) and (5.6) yield a system of five independent equations as follows:

$$x_f^{(p)} - x_f^{(g)} = 0 \tag{5.7}$$

$$y_f^{(p)} - y_f^{(g)} = 0 \tag{5.8}$$

$$z_f^{(p)} - z_f^{(g)} = 0 \tag{5.9}$$

$$n_{fy}^{(p)} n_{fx}^{(g)} - n_{fx}^{(p)} n_{fy}^{(g)} = 0 \tag{5.10}$$

$$n_{fz}^{(p)} n_{fx}^{(g)} - n_{fx}^{(p)} n_{fz}^{(g)} = 0 \tag{5.11}$$

Considering two equations of meshing for gear tooth surfaces, two equations of meshing for pinion tooth surfaces, and Eqs. (5.7)-(5.11), these yield a system of nine independent equations with ten unknowns: l_p, ϕ_p, θ_p, ψ_p, l_g, ϕ_g, θ_g, ψ_g, ϕ_1', and ϕ_2'. Where l_p and ϕ_p are tooth surface parameters of the pinion while l_g and ϕ_g are tooth surface parameters of the gear. If the pinion is a driving gear, the rotational angle ϕ_1' is considered as a given value. Therefore, nine unknown parameters are solved with nine nonlinear equations.

The KEs of a curvilinear gear pair can be calculated by using the following equation:

$$\Delta\phi_2'(\phi_1') = \phi_2'(\phi_1') - \frac{T_p}{T_g}\phi_1', \tag{5.12}$$

where T_p and T_g denote the numbers of teeth of pinion and gear, respectively, while $\phi_2'(\phi_1')$ represents the actual rotational angle of the gear meshing under different assembly conditions, and it is solved by numerical method. $\Delta\phi_2'(\phi_1')$ expresses the KE of a curvilinear gear pair under the given assembly errors.

The contact ratio m_c of the gear pair can be expressed by the following

equation [13]:

$$m_c = \frac{\phi'_{1E} - \phi'_{1B}}{\frac{360^\circ}{T_p}}, \tag{5.13}$$

where ϕ'_{1B} represents the rotational angle of the pinion that corresponds to the point of contact in the beginning of gear pair meshing while ϕ'_{1E} is the rotational angle of the pinion that corresponds to the point of contact at the end of gear meshing for the same pair of profiles. $\phi'_{1E} - \phi'_{1B}$ indicates the rotational angle of the pinion when one pair of teeth is in mesh. The rotational angles ϕ'_{1B} and ϕ'_{1E} can be obtained by TCA simulation computer programs.

5.4 Contact Ellipses

When tooth surfaces are meshed with each other, their instantaneous contact point is spread over an elliptical area owing to elastic deformation. There are two methods to find the contact ellipses. One method is the curvature analysis method, and the other method is surface topology method.

5.4.1 Curvature Analysis Method

The position vector and normal vector of instantaneous contact points at the tooth surfaces of pinion and gear can be obtained by applying the developed TCA computer simulation programs. Based on the procedures proposed in chapter 4, the principal directions and curvatures of the contact points can be obtained. They can be represented by unit vectors $(\mathbf{e}_{\mathrm{I}}^{(1)}, \mathbf{e}_{\mathrm{II}}^{(1)})$ and $(\mathbf{e}_{\mathrm{I}}^{(2)}, \mathbf{e}_{\mathrm{II}}^{(2)})$ and curvatures $(k_{\mathrm{I}}^{(1)}, k_{\mathrm{II}}^{(1)})$ and $(k_{\mathrm{I}}^{(2)}, k_{\mathrm{II}}^{(2)})$, respectively.

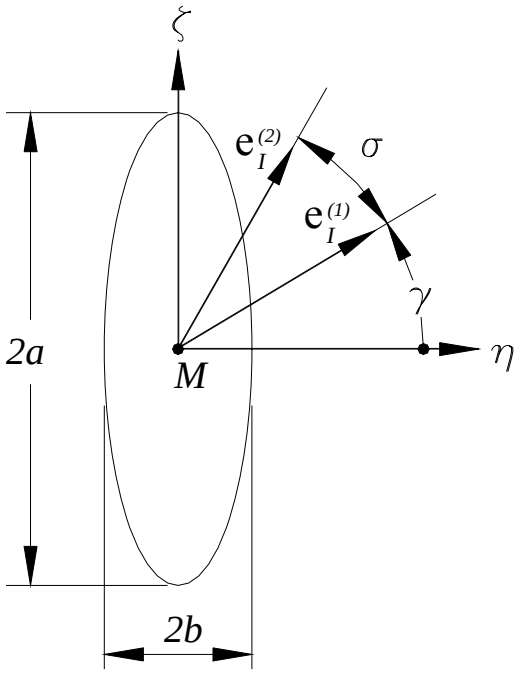

Fig.5.2 Orientation and dimension of contact ellipse

The instantaneous contact of tooth surface at a point is spread over an elliptical area as shown in Fig. 5.2. The unit vectors of any instantaneous contact point, $\mathbf{e}_{\mathrm{I}}^{(1)}$ and $\mathbf{e}_{\mathrm{I}}^{(2)}$, are located on the common tangent plane of the mating tooth surfaces Σ_1 and Σ_2. Symbol a and b represent the half length of the major and minor axes of the contact ellipse, respectively. The orientation of the contact ellipse is determined by the angle γ which is measured from the minor axis of the contact ellipse to the first principal direction of the pinion. The angle γ can be calculated by [12,13]:

$$\tan 2\gamma = \frac{g_2 \sin 2\sigma}{g_1 - g_2 \cos 2\sigma} \tag{5.14}$$

where $g_i = k_{\mathrm{I}}^{(i)} - k_{\mathrm{II}}^{(i)}, \quad i = 1,2$.

Angle σ is formed by the first principal directions of the pinion and gear tooth surfaces $\mathbf{e}_{\mathrm{I}}^{(1)}$ and $\mathbf{e}_{\mathrm{I}}^{(2)}$, and it can be obtained by:

$$\sigma = \cos^{-1}(\mathbf{e}_{\mathrm{I}}^{(1)} \cdot \mathbf{e}_{\mathrm{I}}^{(2)}) \tag{5.15}$$

The half length of the major and minor axes of the contact ellipse, a and b, can be expressed in terms of the elastic deformation δ by[12,13]:

$$a = \left| \frac{\delta}{A_e} \right|^{1/2} \tag{5.16}$$

and $b = \left| \frac{\delta}{B_e} \right|^{1/2}$ (5.17)

where $A_e = \frac{1}{4}[k_{\Sigma}^{(1)} - k_{\Sigma}^{(2)} - (g_1^2 - 2g_1 g_2 \cos 2\sigma + g_2^2)^{1/2}]$,

$B_e = \frac{1}{4}[k_{\Sigma}^{(1)} - k_{\Sigma}^{(2)} + (g_1^2 - 2g_1 g_2 \cos 2\sigma + g_2^2)^{1/2}]$,

and $k_{\Sigma}^{(i)} = k_{\mathrm{I}}^{(i)} + k_{\mathrm{II}}^{(i)}$.

The elastic deformation of the material, δ, is obtained by experiments. Thus, the orientations and dimensions of the contact ellipse of two mating gear tooth surfaces can be determined by utilizing Eqs. (5.14)-(5.17).

5.4.2 Surface Topology Method

Figure 5.3(a) shows that two mating surfaces Σ_p and Σ_g are tangent to each other at their instantaneous contact point O_T, where $\mathbf{n}$ represents the common unit normal vector at contact point O_T, which can be determined by the developed TCA computer simulation programs. Plane T denotes the common tangent plane of the two mating surfaces. The origin of coordinate system $S_T(X_T, Y_T, Z_T)$ and the

instantaneous contact point O_T are coincident. The direction of axis Z_T is defined to coincide with the common unit normal vector $\mathbf{n}$. Thus, the plane $X_T - Y_T$ is the common tangent plane.

The contact ellipses of the gear pair are obtained by using the surface separation topology method [39]. To calculate the separation distance of two mating tooth surfaces, surface coordinates of the mating curvilinear-tooth gear and pinion must be transformed to the same coordinate system $S_T(X_T, Y_T, Z_T)$. Figure 5.3(b) shows the separation distances measured from the tangent plane T to the surfaces Σ_p and Σ_g at point *P*. The separation distance of two mating surfaces can be defined by $d_g + d_p$, where $d_g + d_p$ is equal to $\left|Z_T^{(p)} - Z_T^{(g)}\right|$, measured from any point P on the tangent plane T along its perpendicular direction. $Z_T^{(p)}$ and $Z_T^{(g)}$ represent the coordinates of the Z_T component of points P_p and P_g, respectively. An equal distance-separation line for two mating surfaces is found by defining an auxiliary polar coordinate system (r, θ). Parameter r represents the distance measured outward from the instantaneous contact point O_T to any point P on the common tangent plane T. Parameter θ represents the angle measured from axis X_T to the axis of measurement (distance *r*) on the common tangent plane T. Any point P on the common tangent plane T can be represented in terms of polar coordinate parameters *r* and θ. The amount of the equal distance-separation is set to be 0.00632 mm at this study, since the thickness of the coating paint used for contact pattern tests is 0.00632 mm. Then, the contact patterns (a equal distance-separation line) for two mating tooth surfaces can be found by applying the developed computer programs.

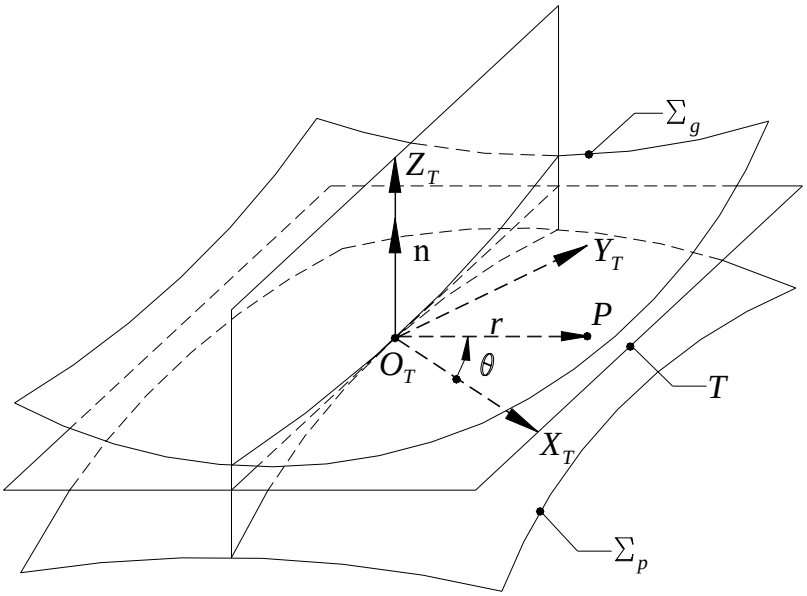

Fig.5.3 (a) Common tangent plane and polar coordinates

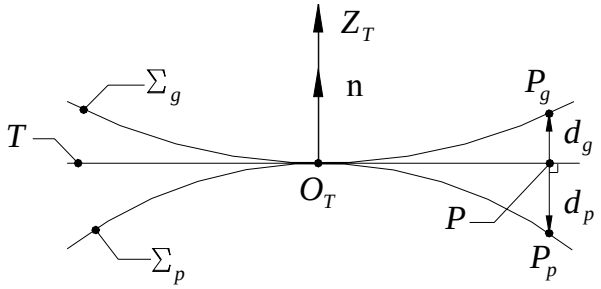

Fig.5.3 (b) Measurement on surface separation

Figure 5.4 shows the relationship among coordinate systems $S_f(X_f, Y_f, Z_f)$, $S_p(X_p, Y_p, Z_p)$, $S_q(X_q, Y_q, Z_q)$, and $S_T(X_T, Y_T, Z_T)$, where coordinate systems $S_p(X_p, Y_p, Z_p)$ and $S_q(X_q, Y_q, Z_q)$ are reference coordinate systems. The two mating tooth surfaces can be represented in the tangent plane coordinate system $S_T(X_T, Y_T, Z_T)$ by applying the following homogeneous coordinate transformation equation:

$$\mathbf{R}_T^{(i)} = M_{Tq} M_{qp} M_{pf} \mathbf{R}_f^{(i)} \qquad (i = p, g), \tag{5.18}$$

where $\mathbf{M}_{pf} = \begin{bmatrix} 1 & 0 & 0 & -p_x \\ 0 & 1 & 0 & -p_y \\ 0 & 0 & 1 & -p_z \\ 0 & 0 & 0 & 1 \end{bmatrix}$,

$$\mathbf{M}_{qp} = \begin{bmatrix} 1 & 0 & 0 & 0 \\ 0 & \cos\sigma & -\sin\sigma & 0 \\ 0 & \sin\sigma & \cos\sigma & 0 \\ 0 & 0 & 0 & 1 \end{bmatrix},$$

$$\mathbf{M}_{Tq} = \begin{bmatrix} \cos\lambda & 0 & -\sin\lambda & 0 \\ 0 & 1 & 0 & 0 \\ \sin\lambda & 0 & \cos\lambda & 0 \\ 0 & 0 & 0 & 1 \end{bmatrix},$$

where superscripts i=p, g denote the pinion and gear, respectively. Symbols p_x, p_y, and p_z designate the coordinate components of the instantaneous contact point of the two mating surfaces represented in the fixed coordinate system $S_f(X_f, Y_f, Z_f)$.

Symbol σ is the angle measured from axis Z_p to axis Z_q while λ represents the angle measured from axis Z_q to axis Z_T. They can be obtained by:

$$\tan\sigma = \frac{n_y}{n_z}, \tag{5.19}$$

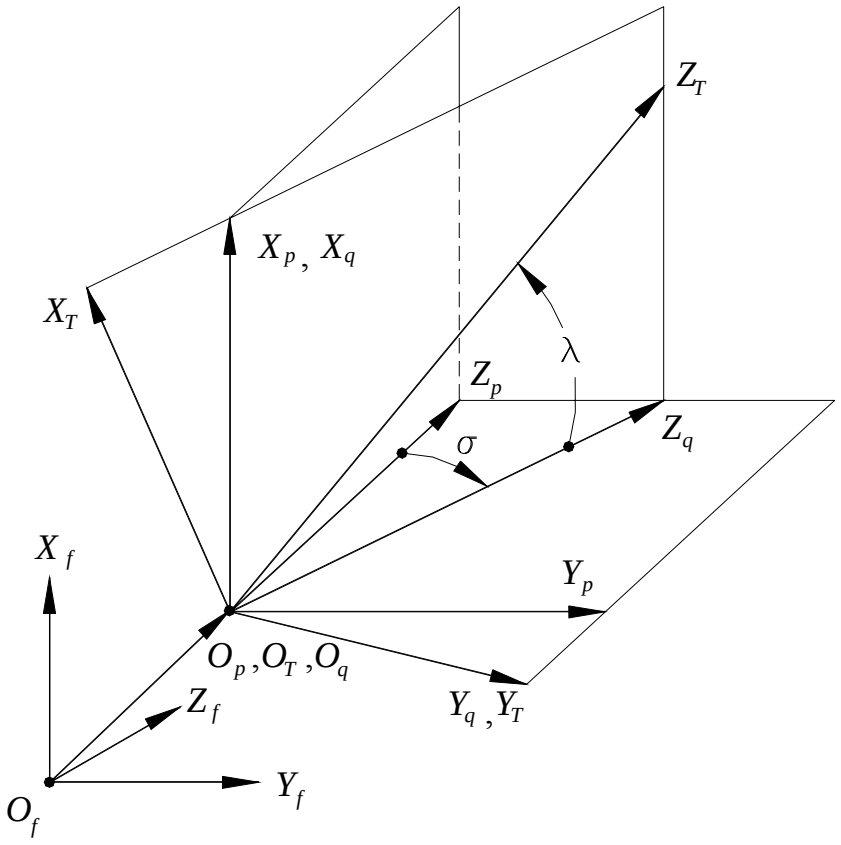

Fig. 5.4 Relationship among coordinate system S_f, S_p, S_q, and S_T

$$\tan\lambda = \frac{n_x}{\sqrt{n_y^2 + n_z^2}}, \tag{5.20}$$

where n_x, n_x, and n_x symbolize the components of the common unit normal vector of the two surfaces at the instantaneous contact point represented in coordinate system $S_f(X_f, Y_f, Z_f)$.

5.5 Numerical Examples for Gear Meshing Simulations

Example 5.1: Curvilinear-tooth gears are meshed under the ideal meshing condition.

The major design parameters of hob cutter, gear, and pinion are shown in Table 5.1. If the pinion and gear are meshing under ideal conditions, it means that the misaligned angles $\Delta\gamma_h = \Delta\gamma_v = 0.0$ degrees, and $\Delta C = \Delta Z = 0.0$ mm. The bearing contacts and KE for ideal meshing condition are shown in Table 5.2. The gear pair induces KE under ideal assembly condition. The bearing contact simulation results $Z_p = Z_g$ =0.0 mm, as shown in Table 5.2, indicates that the contact points are distributed over the middle region of the tooth flank when the gear pair is meshed under ideal assembly conditions. Figure 5.5 illustrates the KE of the gear pair, cut by different outside radii of the hob cutter, under ideal meshing conditions. It is found that the KE of the meshed gear pair decreases as pitch radius r_1 of the hob cutter increases. The contact ratio of the curvilinear-tooth gear pair, calculated by Eq. (5.13) is 1.62. It is similar to that of spur gear pair.

Figure 5.6 depicts the contact path and the contact ellipses on the pinion tooth surface under ideal assembly conditions. The contact ellipses are plotted when the pinion is rotated every 4° from -8° to 8°.

Table 5.1 Some major design parameters for cylindrical gears with circular arc tooth traces

	Hob cutter	Gear	Pinion
Number of teeth	1	40	20
Normal module	3 mm	3 mm	3 mm
Normal pressure angle	20°	20°	20°
Lead angle	2.866°	—	—
Face width	—	40 mm	40 mm
Nominal radius of circular tooth trace	—	110 mm	110 mm
Pitch radius	30 mm	60 mm	30 mm
Outside diameter	67.5 mm	126 mm	66 mm

Table 5.2 kinematic errors and bearing contacts under the ideal meshing condition ($R_{cp} = R_{cg} = 110$ mm)

ϕ_1' (deg.)	ϕ_2' (deg.)	l_p (mm)	Z_p (mm)	l_g (mm)	Z_g (mm)	KE(arc-sec.)
-10.000	-4.999	4.301	0.000	9.474	0.000	4.249
-8.000	-3.999	4.658	0.000	9.117	0.000	3.036
-6.000	-2.999	5.016	0.000	8.761	0.000	2.006
-4.000	-2.000	5.373	0.000	8.404	0.000	1.158
-2.000	-1.000	5.730	0.000	8.048	0.000	0.489
0.000	0.000	6.087	0.000	7.691	0.000	0.000
2.000	1.000	6.444	0.000	7.334	0.000	-0.311
4.000	2.000	6.801	0.000	6.977	0.000	-0.444
6.000	3.000	7.158	0.000	6.620	0.000	-0.399
8.000	4.000	7.515	0.000	6.263	0.000	-0.176
10.000	5.000	7.871	0.000	5.906	0.000	0.225

Figure 5.7 shows the relationship between the nominal radius of circular arc tooth trace R_c and the ratio of the major and minor axes of the contact ellipse a/b when the normal pressure angles are 20 degrees and 25 degrees, respectively. Based on Fig. 5.7, when the normal pressure angles equal 20 degrees and 25 degrees, the ratios a/b are 43.2 and 42.3, respectively, under nominal radius R_c=110 mm. It is found that the ratio a/b is proportional to the nominal radius of circular arc tooth trace R_c.

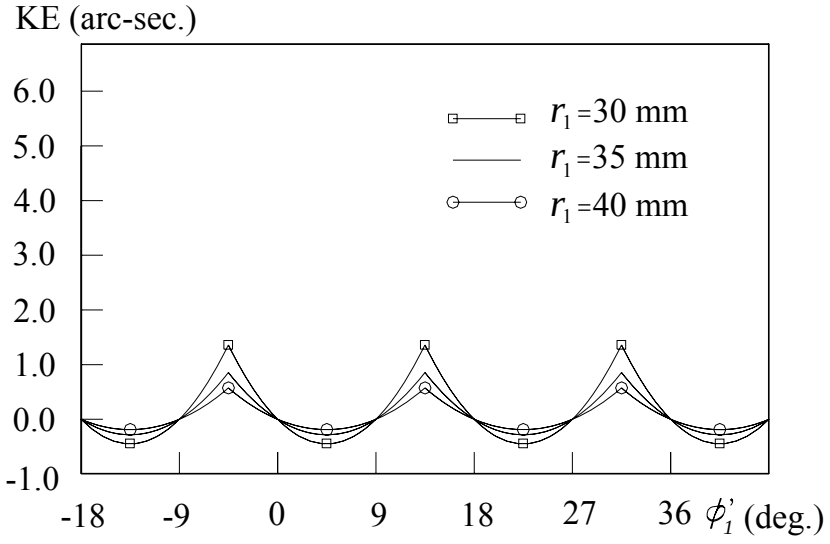

Fig. 5.5 Kinematic errors of the curvilinear-tooth gear pair under ideal meshing condition

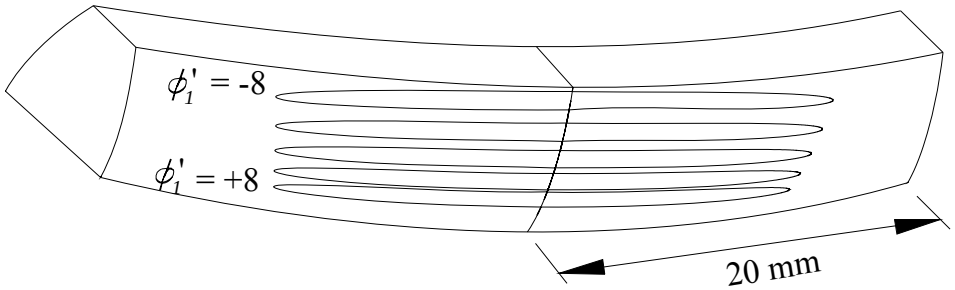

Fig. 5.6 Contact ellipses and bearing contacts on the pinion surface under ideal assembly condition

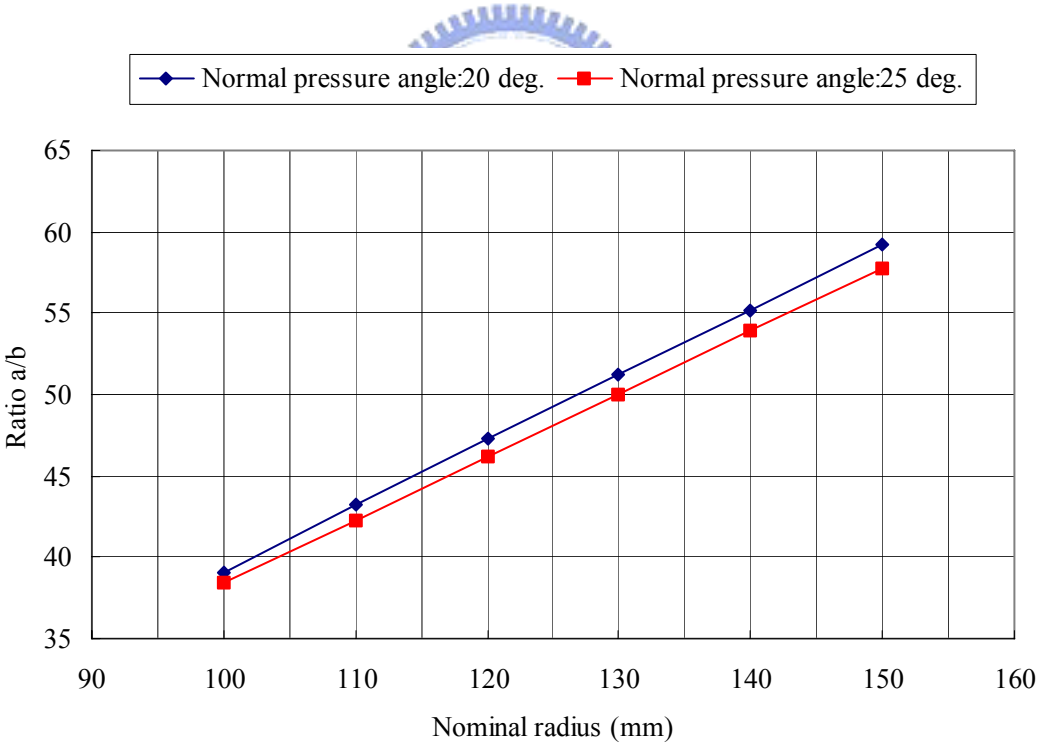

Fig. 5.7 Relationship between the ratio a/b and nominal radius R_c

Table 5.3 kinematic errors and bearing contacts due to horizontal axial misalignment $\Delta\gamma_h = 3'$ ($R_{cp} = R_{cg} = 110$ mm)

ϕ_1' (deg.)	ϕ_2' (deg.)	l_p (mm)	Z_p (mm)	l_g (mm)	Z_g (mm)	KE(arc-sec.)
-10.000	-4.998	4.460	10.672	9.322	10.667	3.859
-8.000	-3.999	4.816	10.569	8.966	10.565	2.726
-6.000	-2.999	5.173	10.467	8.610	10.463	1.775
-4.000	-1.999	5.529	10.365	8.254	10.362	1.004
-2.000	-0.999	5.886	10.263	7.898	10.261	0.413
0.000	0.000	6.242	10.162	7.542	10.160	0.000
2.000	0.999	6.599	10.061	7.186	10.060	-0.235
4.000	1.999	6.955	9.960	6.829	9.960	-0.292
6.000	2.999	7.312	9.860	6.473	9.861	-0.172
8.000	4.000	7.668	9.760	6.116	9.762	0.126
10.000	5.000	8.024	9.660	5.760	9.663	0.601

Example 5.2: Curvilinear-tooth gears are meshed under a horizontal axial-misalignment $\Delta\gamma_h = 3'$.

The gear pair has a horizontal axial-misalignment $\Delta\gamma_h = 3'$. Table 5.3 lists the analysis results of bearing contacts and KEs using the same gear design parameters as those of given in Example 5.1. The contact points are distributed near the cross section Z_p=10 mm. Comparing the bearing contacts of Example 5.1 and Example 5.2, it is found that the bearing contacts of the gear pair shift from cross section Z_p =0 mm to Z_p =10 mm as the gear pair is meshed with a horizontal axial-misalignment $\Delta\gamma_h = 3'$. The variation of KE is small in comparison with that of Example 5.1.

Example 5.3: Curvilinear-tooth gears are meshed under the ideal meshing condition (R_{cp} =110 mm and R_{cg} =113 mm).

The major design parameters are chosen the same as those of given in Example 5.1, except that the nominal radii R_{cp} and R_{cg} are 110 mm and 113 mm, respectively. Two mating curvilinear-tooth gears are meshed under ideal assembly condition. There are two methods to estimate the contact ellipses in this Example. The contact path and contact ellipses of the gear pair under ideal assembly condition are shown in Fig. 5.8. The contact ellipses with green color are estimated by surface topology method while the red one is estimated by curvature analysis method. The contact points are distributed at the middle section of the tooth flank in this example. Figure 5.8 shows that the contact ellipses calculated by different methods are very similar.

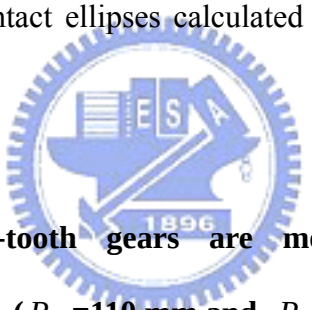

Example 5.4: Curvilinear-tooth gears are meshed under a horizontal axial-misalignment $\Delta\gamma_h = 3'$ (R_{cp} =110 mm and R_{cg} =113 mm).

The gear design parameters are chosen the same as those of given in Example 5.3. The horizontal axial-misalignment of the gear $\Delta\gamma_h = 3'$ is considered when two mating curvilinear-tooth gears are meshed. The bearing contacts and KEs of the gear pair under the prescribed horizontal axial-misalignment are shown in Table 5.4. Based on the analysis results, the contact points are distributed near the cross section Z_p=3.5 mm and the KEs of the mating gear pair are similar to those of Example 5.1. The bearing contacts and contact ellipses are depicted in Fig. 5.9. It is found that the bearing contacts are localized and shifted from the cross-section Z_p=10 mm back to the cross-section Z_p=3.5 mm of the tooth flank. This case implies that the shift of

bearing contacts caused by horizontal axial-misalignment can be reduced by properly choosing the nominal radii of circular arc tooth trace R_{cp} and R_{cg}.

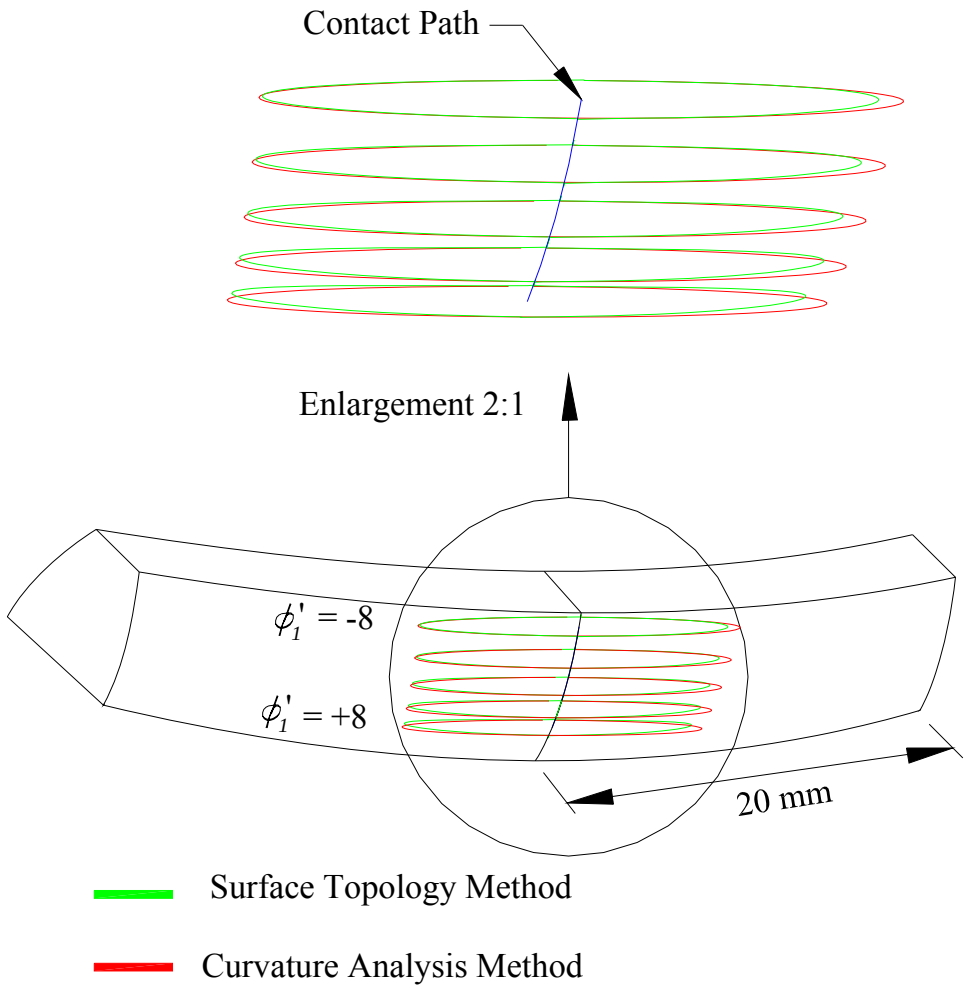

Fig. 5.8 Contact ellipses and bearing contacts on the pinion surface under ideal assembly condition

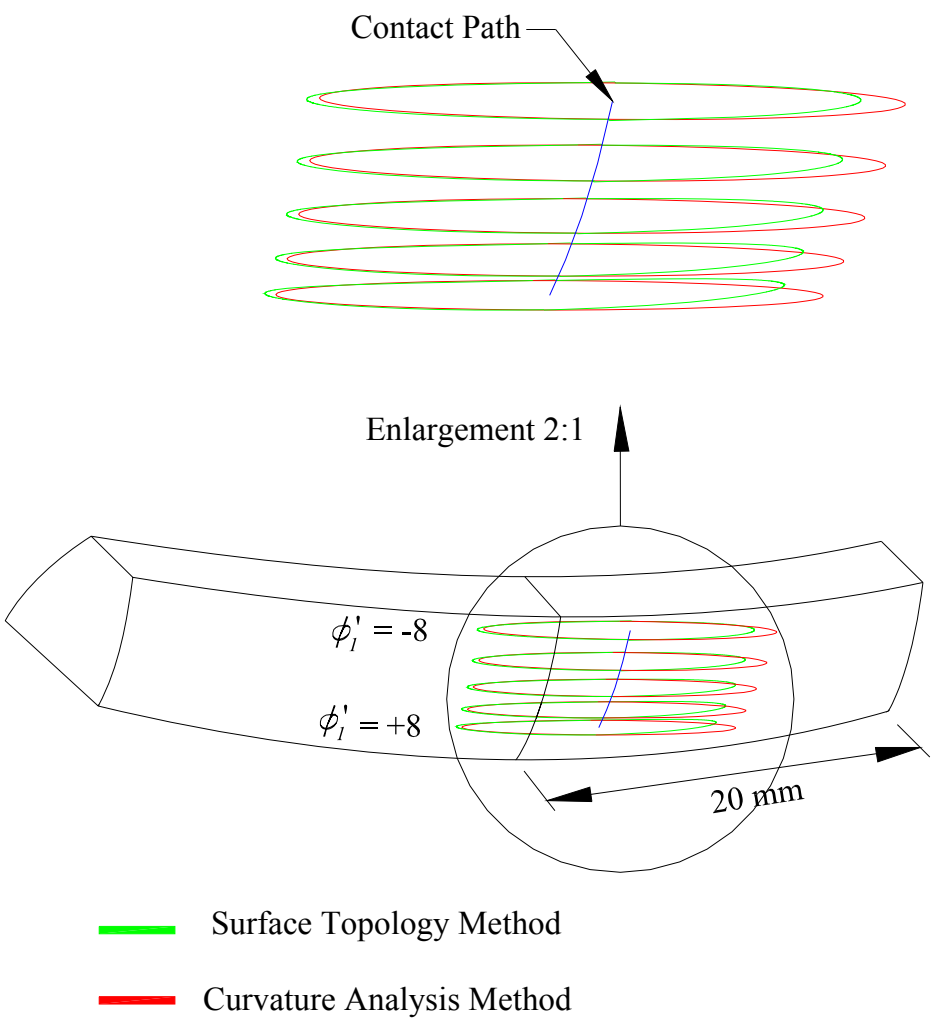

Fig.5.9 Contact ellipses and bearing contacts on the pinion surface under horizontal axial-misalignment $\Delta\gamma_h = 3'$

Table 5.4 kinematic errors and bearing contacts due to horizontal axial misalignment $\Delta\gamma_h = 3'$ ($R_{cp} = 110$ mm and $R_{cg} = 113$ mm)

ϕ_1' (deg.)	ϕ_2' (deg.)	l_p (mm)	Z_p (mm)	l_g (mm)	Z_g (mm)	KE(arc-sec.)
-10.000	-4.998	4.319	3.727	9.456	3.721	4.203
-8.000	-3.999	4.677	3.691	9.099	3.686	2.999
-6.000	-2.999	5.034	3.655	8.743	3.651	1.979
-4.000	-1.999	5.391	3.620	8.386	3.617	1.139
-2.000	-0.999	5.748	3.585	8.030	3.582	0.480
0.000	0.000	6.105	3.550	7.673	3.548	0.000
2.000	0.999	6.462	3.515	7.316	3.514	-0.302
4.000	1.999	6.819	3.480	6.959	3.480	-0.426
6.000	2.999	7.176	3.445	6.603	3.446	-0.372
8.000	3.999	7.532	3.410	6.246	3.412	-0.140
10.000	5.000	7.889	3.376	5.889	3.378	0.270

Table 5.5 kinematic errors and bearing contacts due to vertical axial misalignment $\Delta\gamma_v = 3'$ ($R_{cp} = 110$ mm and $R_{cg} = 113$ mm)

ϕ_1' (deg.)	ϕ_2' (deg.)	l_p (mm)	Z_p (mm)	l_g (mm)	Z_g (mm)	KE(arc-sec.)
-10.000	-4.998	4.301	0.380	9.474	0.352	4.248
-8.000	-3.999	4.659	0.377	9.117	0.349	3.036
-6.000	-2.999	5.016	0.373	8.761	0.345	2.006
-4.000	-1.999	5.373	0.369	8.404	0.342	1.157
-2.000	-0.999	5.730	0.366	8.048	0.339	0.489
0.000	0.000	6.087	0.362	7.691	0.335	0.000
2.000	0.999	6.444	0.359	7.334	0.332	-0.311
4.000	1.999	6.801	0.355	6.977	0.329	-0.443
6.000	2.999	7.158	0.351	6.620	0.326	-0.398
8.000	3.999	7.515	0.348	6.263	0.322	-0.176
10.000	5.000	7.872	0.345	5.906	0.319	0.225

Example 5.5: Curvilinear-tooth gears are meshed under a vertical axial-misalignment $\Delta\gamma_v = 3'$ (R_{cp}=110 mm and R_{cg}=113 mm).

The gear design parameters are chosen the same as those of given in Example 5.3. The gear pair is meshed with vertical axial-misalignment $\Delta\gamma_v = 3'$. The bearing contacts and KEs of the gear pair under the prescribed vertical axial-misalignment are listed in Table 5.5. In this case the contact points are distributed near the cross section Z_p= 0.36 mm. The KEs of the curvilinear-tooth gears induced by vertical axial-misalignments are similar to those induced by horizontal axial- misalignments. Figure 5.10 illustrates the bearing contacts and contact ellipses of the curvilinear-tooth gear pair on pinion tooth surfaces under vertical axial-misalignments $\Delta\gamma_v = 3'$.

Table 5.6 kinematic errors and bearing contacts due to center distance variation $\Delta C = 0.2$ mm ($R_{cp} = 110$ mm and $R_{cg} = 113$ mm)

ϕ_1' (deg.)	ϕ_2' (deg.)	l_p (mm)	Z_p (mm)	l_g (mm)	Z_g (mm)	KE(arc-sec.)
-10.000	-4.998	4.239	0.000	9.325	0.000	4.180
-8.000	-3.999	4.596	0.000	8.968	0.000	2.978
-6.000	-2.999	4.953	0.000	8.612	0.000	1.960
-4.000	-1.999	5.311	0.000	8.255	0.000	1.125
-2.000	-0.999	5.668	0.000	7.899	0.000	0.472
0.000	0.000	6.025	0.000	7.542	0.000	0.000
2.000	0.999	6.382	0.000	7.185	0.000	-0.292
4.000	1.999	6.739	0.000	6.828	0.000	-0.404
6.000	2.999	7.096	0.000	6.471	0.000	-0.337
8.000	3.999	7.452	0.000	6.114	0.000	-0.090
10.000	5.000	7.809	0.000	5.757	0.000	0.337

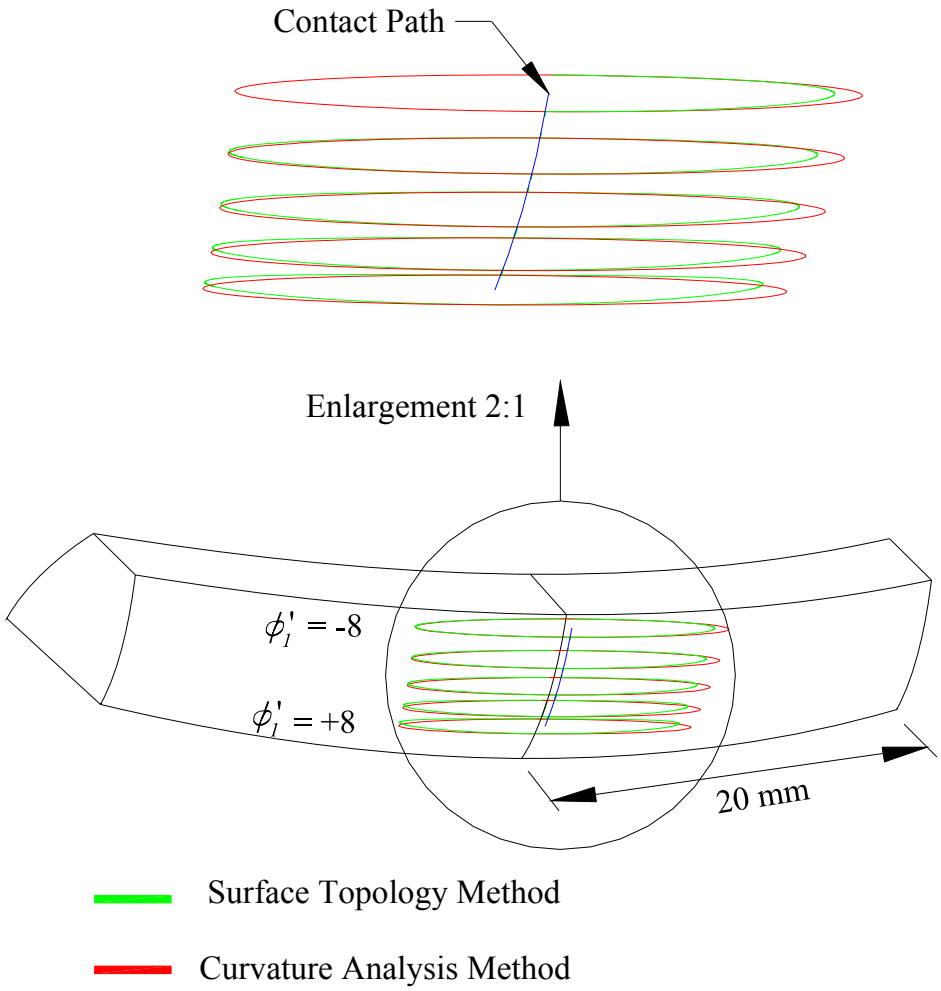

Fig.5.10 Contact ellipses and bearing contacts on the pinion surface under vertical axial-misalignment $\Delta\gamma_v = 3'$

Table 5.7 kinematic errors and bearing contacts due to assembly error $\Delta Z = 0.1$ mm ($R_{cp} = 110$ mm and $R_{cg} = 113$ mm)

ϕ_1' (deg.)	ϕ_2' (deg.)	l_p (mm)	Z_p (mm)	l_g (mm)	Z_g (mm)	KE(arc-sec.)
-10.000	-4.998	4.321	-3.771	9.454	3.871	4.200
-8.000	-3.999	4.678	-3.734	9.098	3.834	2.997
-6.000	-2.999	5.035	-3.698	8.741	3.798	1.977
-4.000	-1.999	5.392	-3.663	8.385	3.763	1.138
-2.000	-0.999	5.749	-3.627	8.028	3.727	0.480
0.000	0.000	6.106	-3.591	7.672	3.691	0.000
2.000	0.999	6.463	-3.556	7.315	3.656	-0.301
4.000	1.999	6.820	-3.520	6.958	3.620	-0.424
6.000	2.999	7.177	-3.485	6.601	3.585	-0.370
8.000	3.999	7.534	-3.450	6.244	3.550	-0.138
10.000	5.000	7.890	-3.415	5.887	3.515	0.273

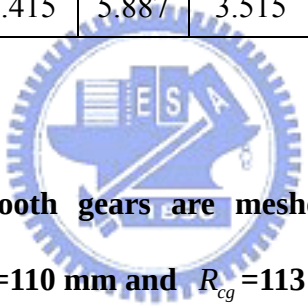

Example 5.6: Curvilinear-tooth gears are meshed under a center distance variation $\Delta C = 0.2$ mm (R_{cp} =110 mm and R_{cg} =113 mm).

Table 5.6 lists the analysis results of bearing contacts and KEs using the same gear design parameters as those of given in Example 5.3 with $\Delta C = 0.2$ mm. The contact points of the curvilinear-tooth gear pair are dislocated and KEs are similar to those of Example 5.4 or Example 5.5. Table 5.6 illustrates that the contact points are still distributed over the middle region of the tooth flank.

Example 5.7: Curvilinear-tooth gears are meshed with assembly error $\Delta Z = 0.1$ mm (R_{cp} =110 mm and R_{cg} =113 mm).

Table 5.7 lists the analysis results of bearing contacts and KEs using the same gear design parameters as those of given in Example 5.3 with $\Delta Z = 0.1$ mm. The

contact points of the curvilinear-tooth gear pair are dislocated and KEs are similar to those of Example 5.4. It is found that the bearing contacts of the gear pair shift from cross section Z_p=0 mm to Z_p= -3.5 mm as the gear pair is meshed with assembly error $\Delta Z = 0.1$ mm. Figure 5.11 illustrates the contact path and contact ellipses of the curvilinear-tooth gear pair on pinion tooth surfaces with assembly error $\Delta Z = 0.1$ mm.

Example 5.8: Curvilinear-tooth gears are meshed under $\Delta\gamma_h = 3'$, $\Delta\gamma_v = 3'$, and ΔC = 0.2 mm (R_{cp} =110 mm and R_{cg} =113 mm).

The gear design parameters are also chosen the same as those of given in Example 5.3. When two mating gears are meshed under $\Delta\gamma_h = 3'$, $\Delta\gamma_v = 3'$, and $\Delta C = 0.2$mm, the analysis results are shown in Table 5.8. The contact points are

Table 5.8 kinematic errors and bearing contacts under $\Delta\gamma_h = 3'$, $\Delta\gamma_v = 3'$, and $\Delta C = 0.2$ mm ($R_{cp} = 110$ mm and $R_{cg} = 113$ mm)

ϕ_1' (deg.)	ϕ_2' (deg.)	l_p (mm)	Z_p (mm)	l_g (mm)	Z_g (mm)	KE(arc-sec.)
-10.000	-4.998	4.270	4.792	9.297	4.758	4.104
-8.000	-3.999	4.628	4.746	8.940	4.713	2.917
-6.000	-2.999	4.985	4.699	8.584	4.667	1.915
-4.000	-1.999	5.342	4.653	8.227	4.622	1.095
-2.000	-0.999	5.699	4.607	7.871	4.577	0.457
0.000	0.000	6.056	4.561	7.514	4.533	0.000
2.000	0.999	6.413	4.516	7.158	4.488	-0.277
4.000	1.999	6.769	4.470	6.801	4.444	-0.375
6.000	2.999	7.126	4.425	6.444	4.400	-0.293
8.000	3.999	7.483	4.380	6.087	4.356	-0.032
10.000	5.000	7.839	4.335	5.730	4.312	0.410

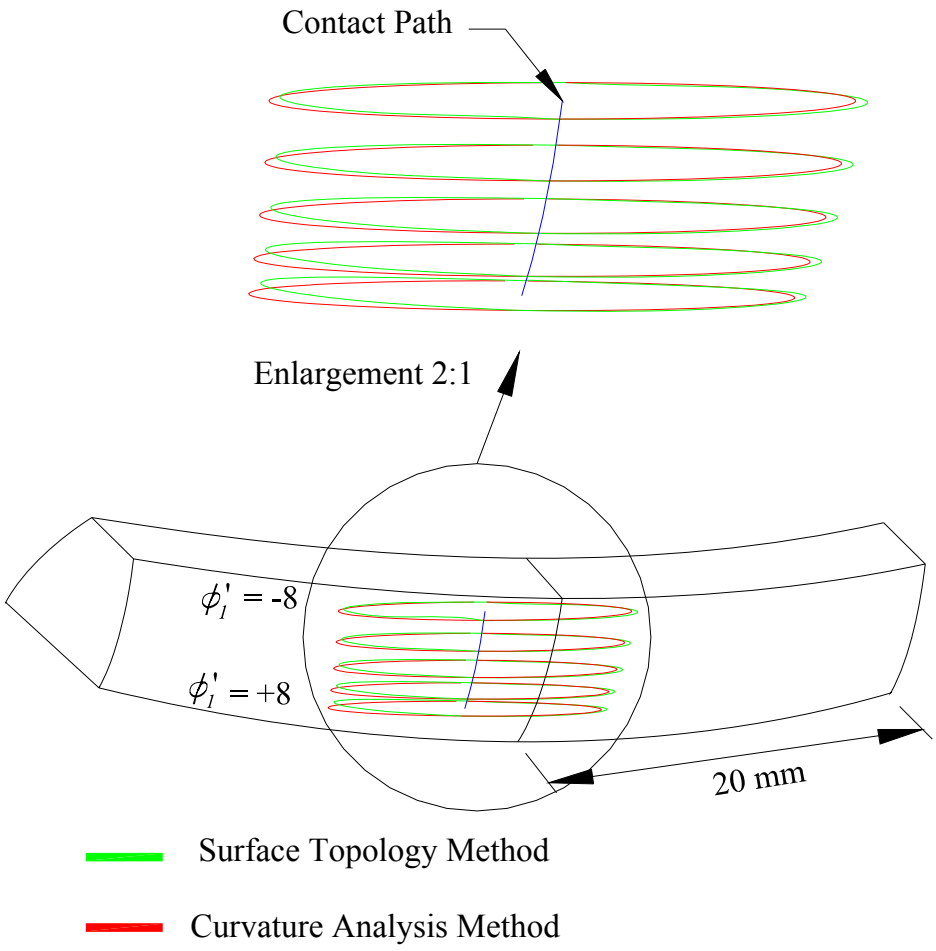

Fig.5.11 Contact ellipses and bearing contacts on the pinion surface under an assembly error $\Delta Z = 0.1$ mm

Table 5.9 kinematic errors and bearing contacts under $\Delta\gamma_h = 3'$, $\Delta\gamma_v = 3'$, $\Delta C = 0.2$ mm, and $\Delta Z = 0.1$ mm ($R_{cp} = 110$ mm and $R_{cg} = 113$ mm)

ϕ_1' (deg.)	ϕ_2' (deg.)	l_p (mm)	Z_p (mm)	l_g (mm)	Z_g (mm)	KE(arc-sec.)
-10.000	-4.998	4.239	0.393	9.325	-0.259	4.180
-8.000	-3.999	4.596	0.389	8.969	-0.256	2.978
-6.000	-2.999	4.954	0.385	8.612	-0.253	1.960
-4.000	-1.999	5.311	0.382	8.255	-0.251	1.125
-2.000	-0.999	5.668	0.378	7.899	-0.248	0.472
0.000	0.000	6.025	0.374	7.542	-0.245	0.000
2.000	0.999	6.382	0.371	7.185	-0.243	-0.292
4.000	1.999	6.739	0.367	6.828	-0.240	-0.404
6.000	2.999	7.096	0.363	6.471	-0.238	-0.337
8.000	3.999	7.453	0.360	6.115	-0.236	-0.090
10.000	5.000	7.809	0.356	5.757	-0.233	0.337

distributed near the cross section Z_p = 4.5 mm. Figure 5.12 illustrates the bearing contacts and contact ellipses of the curvilinear-tooth gear pair on pinion tooth surfaces. It is found that the bearing contacts are also localized near the cross section Z_p = 4.5 mm.

Example 5.9: Curvilinear-tooth gears are meshed under $\Delta\gamma_h = 3'$, $\Delta\gamma_v = 3'$, and ΔC = 0.2 mm, and ΔZ = 0.1 mm (R_{cp} =110 mm and R_{cg} =113 mm).

The gear design parameters are also chosen the same as those of given in Example 5.3. When two mating gears are meshed under $\Delta\gamma_h = 3'$, $\Delta\gamma_v = 3'$, $\Delta C = 0.2$mm, and $\Delta Z = 0.1$ mm, the analysis results are shown in Table 5.9. The contact points are distributed near the cross section Z_p = 0.37 mm. Figure 5.13 illustrates the bearing contacts and contact ellipses of the curvilinear-tooth gear pair

on pinion tooth surfaces. It is found that the bearing contacts are localized near the middle region of the tooth flank.

5.6 Remarks

The bearing contact and KEs of the curvilinear-tooth gears are investigated by applying the developed TCA computer programs. The contact ellipses of the curvilinear-tooth gear pair under different assembly conditions can be estimated by utilizing the curvature analysis method or surface topology method. According to the numerical results, the following conclusions can be drawn:

(1) The gear pair, generated by a ZA worm-type hob cutter, induces KEs under ideal assembly condition. However, the level of KEs of the gear pair is small. The bearing contacts are localized in the middle region of the tooth flank under the ideal assembly condition.

(2) The KEs of the meshed gear pair under ideal assembly condition decreases when the gear pair is generated by a larger pitch radius of the hob cutter r_1.

(3) The curvilinear-tooth gear pair induces KEs while the gear pair is meshed with center distance variations and the bearing contacts are localized in the middle region of the tooth flank.

(4) The KE of the gear pair is not sensitive to axial misalignments because the contact type of the proposed curvilinear-tooth gear pair is in point contacts.

(5) The bearing contact can be localized near the middle region of the tooth flank by properly choosing a nominal radius of circular arc tooth trace. The ratio of the major and minor axes of the contact ellipse a/b is proportional to the nominal radius of circular arc tooth trace.

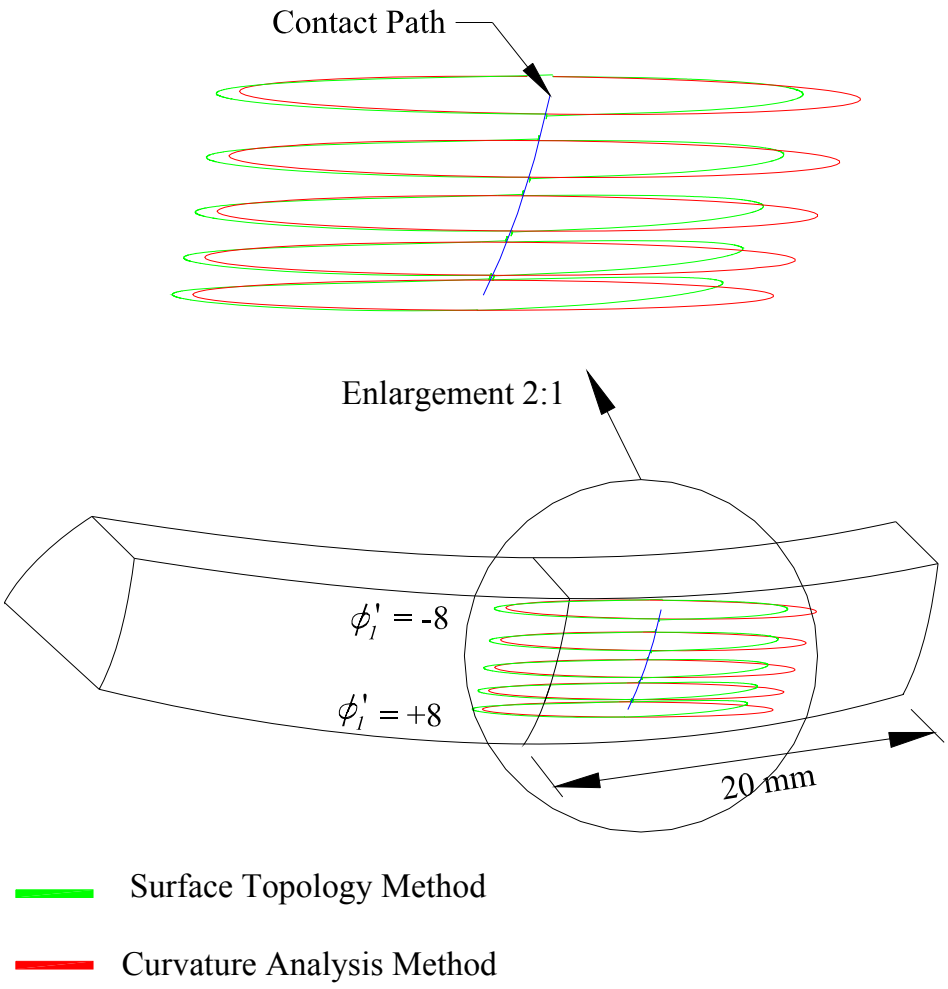

Fig.5.12 Contact ellipses and bearing contacts on the pinion surface with assembly errors $\Delta\gamma_h = 3'$, $\Delta\gamma_v = 3'$ and $\Delta C = 0.2$ mm

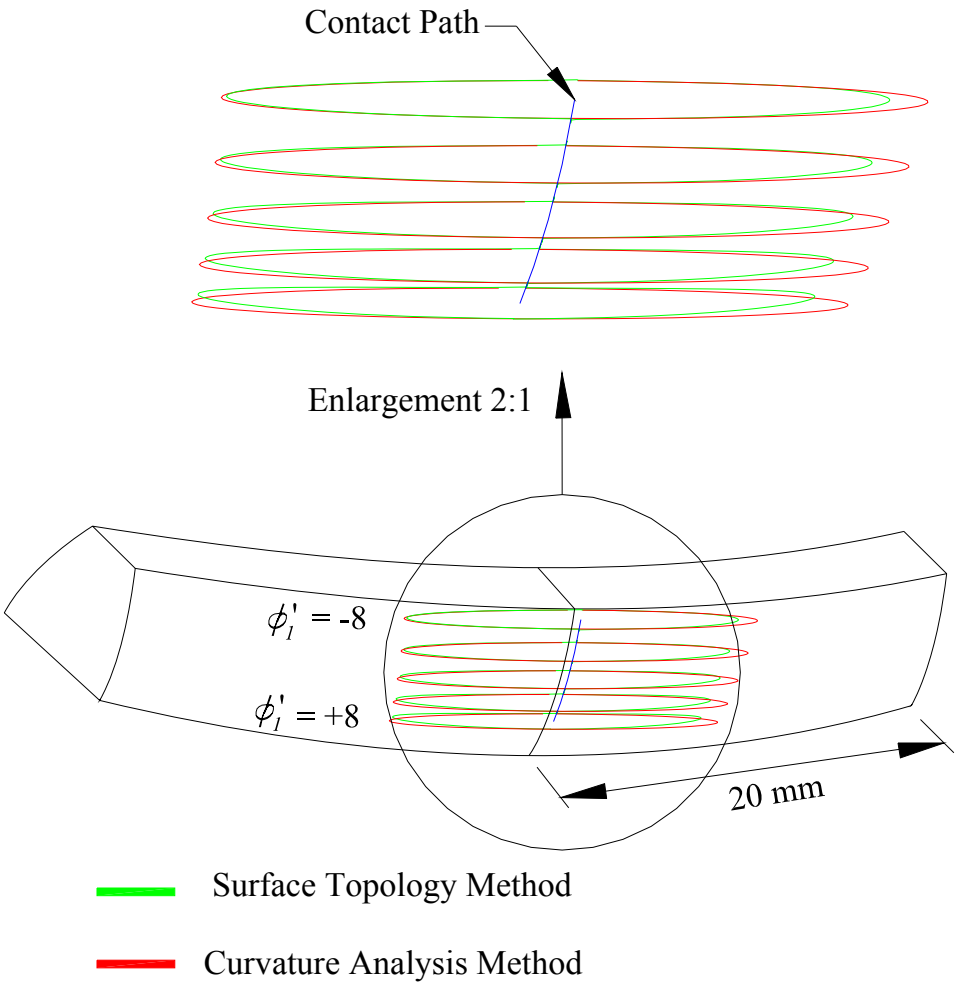

Fig.5.13 Contact ellipses and bearing contacts on the pinion surface with assembly errors $\Delta\gamma_h = 3'$, $\Delta\gamma_v = 3'$, $\Delta C = 0.2$ mm and $\Delta Z = 0.1$ mm

CHAPTER 6

Finite Element Stress Analysis

6.1 Introduction

The finite element method (FEM) is an effective tool for the determination of elastic tooth deformations and stress analysis. Many researchers applied FEM to study tooth deflection and stress distribution for various types of gear drives [40-43]. Tsay and Fong [44] and Litvin et al. [45] applied loads directly to the contact ellipses or contact lines on tooth surfaces obtained from TCA to estimate stress contours. In some literature, contact boundary conditions are simulated with gap elements as a three-dimensional stress analysis is performed [46-48]. Celik [49] estimated the gear teeth deflections and stresses, and compared the analysis results of three teeth model with whole body model. The analysis results are very similar for both models. Some researchers discussed the contact and bending stresses of tooth surfaces by using FEA softwares [50-52]. The results calculated by FEM are compared with those obtained experimentally with strain gages [53-54].

In this chapter, a multi-tooth meshing model is performed to simulate the bearing contacts of the mating gear pair. The location of bearing contacts under a given load is investigated, and the tooth stress distribution of the proposed curvilinear-tooth gear pairs is also calculated based on the FEM and the general-purpose FEA simulation software, ABAQUS/Standard 6.4. A PC version of analysis simulation program, running on windows 2000 operating system, is used to obtain the numerical solution for the contact problem by applying the nonlinear static analysis.

6.2 Finite Element Contact Analysis Model

Application of FEM requires the development of the finite element analysis model formed by finite element meshes, the definition of contacting surfaces, the specification of surface interaction model, and the establishment of boundary conditions. In this study, The following assumptions have been made: (1) a pair of gears with three-teeth model is meshed to perform the stress analysis, (2) both materials of gear and pinion are considered as isotropic and homogeneous materials, (3) small displacement and small sliding between the contact surfaces are assumed, and (4) Thermal stress is ignored.

6.2.1 Finite Element Meshes

The tooth surfaces of the curvilinear-tooth gear are complicated surfaces. It is difficult to establish a solid model for this type of gearing by applying commercial CAD computer softwares such as I-DEAS or ProEngineer. A mesh-generation program has been developed in this study to generate nodal points of the tooth surfaces and to discretize the geometric models of the pinion and the gear tooth surfaces by finite elements for FEA. The developed mesh-generation program allows one to adjust the mesh density and the number of elements to meet specific requirements.

The nodal coordinates lying on tooth surfaces, including the region of active profiles and fillets, are determined analytically by applying the developed mathematical model of the curvilinear-tooth gear. Therefore, the lost of accuracy due to the development of FE models using CAD computer programs is avoided. Besides, the location of contact points on pinion and gear can be obtained from TCA computer programs.

Establishing a finite element analysis model requires properly choosing a suitable element type and then generating the corresponding mesh system. In this study, the three-dimensional solid element in incompatible modes, C3D8I [50], having eight nodes and six faces, is employed to discretize the geometric models of the pinion and the gear tooth surfaces. These elements are the first-order elements that are enhanced by incompatible modes to improve their bending behavior. The discretization of pinion and gear teeth for a pair of three-teeth finite element model is represented in Fig. 6.1. The possible contact regions in the central section of the face width are discretized by finer meshes.

6.2.2 Surface Definition and Interaction Properties

The contact definition in ABAQUS/Standard has two parts: the definition of the surfaces and the definition of the interaction between surfaces. Generally, the master surface should be chosen as the surface of the stiffer body if the two surfaces are on structures with comparable stiffness, or as the surface with the coarser meshes. The nodes of the master surface can penetrate into the slave surface; however, the nodes on slave surfaces are constrained not to penetrate into the master surface during the analysis processes. The convex sides of pinion tooth surfaces have been chosen as the slave surfaces while the concave sides of gear tooth surfaces as the master one considering that the surfaces of the gear tooth are harder than that of the pinion tooth.

Two options, “small sliding” and “no friction”, in an ABAQUS contact simulation should be specified to define the interaction between the contact pair. In this study, the friction coefficient is given as zero by assuming that the gears are meshed under good lubrication conditions.

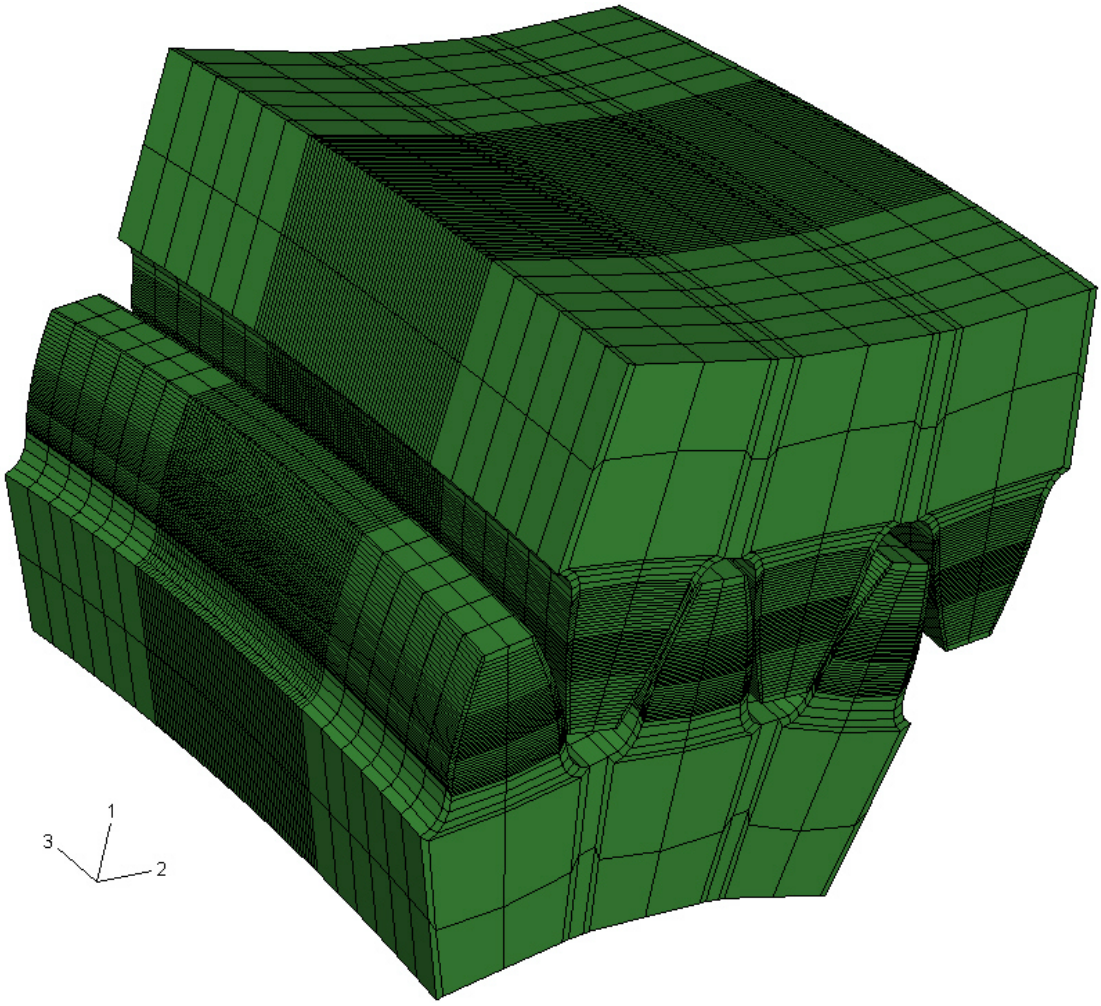

Fig. 6.1 A pair of three teeth finite element meshing model

6.2.3 Boundary Conditions and Loads

The Incompatible mode element, C3D8I, has three degrees of freedom (DOF) active at each node: translations in the 1-, 2-, and 3- directions. In this study, the nodes on the two lateral sides and bottom of the gear's base are considered fixed, as shown in Fig. 6.2. Therefore, these nodes have zero displacement in the degrees of freedom 1-, 2-, and 3-directions. In addition, the nodes on the bottom of the pinion's base are connected to the pinion's rotational axis by rigid beam elements, and the nodes on the pinion's rotational axis are constrained in a way such that the pinion can rotate about its rotational axis only. The torque is applied directly to the remaining DOF at the pinion's rotational axis to make the tooth surfaces of gear and pinion contact with each other. The FEA model to simulate the tooth contact with a pair of three-meshing-teeth gears with boundary conditions is depicted in Fig. 6.2.

Table 6.1 Major design parameters for the curvilinear-tooth gear

	Hob cutter	Gear	Pinion
Number of teeth	1	57	31
Normal module	3	3	3
Normal pressure angle	20°	20°	20°
Lead angle	2.866°	—	—
Face width	—	30 mm	30 mm
Nominal radius of circular tooth trace	—	113 mm	110 mm
Pitch radius	30 mm	85.5 mm	46.5 mm
Outside diameter	67.5 mm	177 mm	99 mm

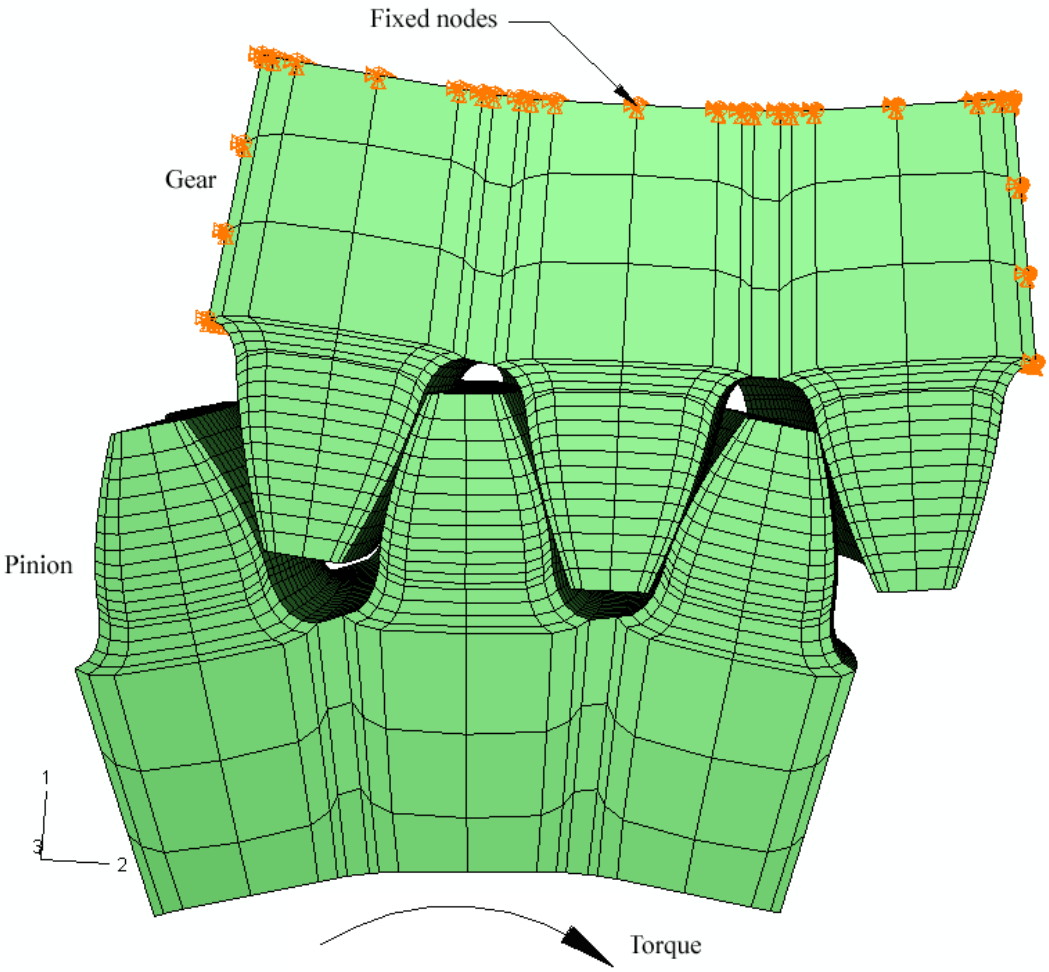

Fig. 6.2 FEA model of three pair of meshing teeth

6.3 Simulation Results and Discussions

The major design parameters of the curvilinear-tooth gear pair are shown in Table 6.1. The pinion and gear are carbon steel with a hardness of 350 Brinell tooth surface and through-hardened core. The material properties are listed in Table 6.2. The generation of the finite element analysis model is performed automatically using the data as shown in Table 6.3. A torque of 200 N-m is applied to the pinion's rotational axis. The accomplished stress analysis enables to obtain the von Mises stresses, and be labeled by symbols "S, Mises" in the contour plots. The unit used for the stress distribution is N/mm^2.

Figures 6.3 to 6.5 show the distributions of the bearing contacts, contact stresses and bending stresses obtained by FEA for the mating gear pair. Two teeth may be meshed near the mean point of the path of contact due to elastic deformation of the tooth. The variations of contact stresses and bending stresses during one tooth of gear pair meshing are illustrated in Fig. 6.6 and Fig. 6.7, respectively. According to the TCA simulation results, the pitch points of tooth surfaces are meshed when the pinion's rotational angle is 2.899°. It is obvious that the maximum bending stress occur when the contact point is near the pitch point as shown in Fig. 6.7.

Table 6.2 Material properties for the gears

Medium Carbon Steel	AISI 1045
Modules of Elasticity (MPa)	205.0E3
Poisson's Ratio	0.29
Density (Kg/mm^3)	78.5E-7
Hardness (H_B)	350
Allowable Contact Stress (MPa) (Source: AGMA 2001-C95)	980
Allowable Bending Stress (MPa) (Source: AGMA 2001-C95)	275

Table 6.3 Finite element analysis model for the investigated gear pair

	Gear	Pinion
Total number of elements	95,616	
Total number of nodes	122,713	
Element type	C3D8I	
Contact pair	Master surface	Slave surface
Interaction between surfaces	Small sliding, no friction	
Boundary condition	Fixed	Torque applied 200 N-m

The maximum contact stresses on gear concave surface and pinion convex surface are 754.5 MPa and 760.3 MPa, while the maximum bending stresses are 170.3 MPa, and 175.2 MPa respectively. The allowable contact stress and bending stress are 980 MPa and 275 MPa, respectively, as shown in Table 6.2. Therefore, the factor of safety of the gears in contact is 1.29, and the factor of safety of the gears in bending is 1.57.

Figure 6.8 shows the variations of contact and bending stresses of the gear under different nominal radius R_c. Consequently, by increasing the nominal radius R_c reduces the contact stresses and bending stresses due to a larger contact area of the gear tooth surface. Figure 6.9 illustrates the distributions of contact stress when the nominal radius R_c is 50000 mm. The profile of a curvilinear-tooth gear is similar to that of a spur gear when the nominal radius is very large. In this case, the contact pattern covers the whole tooth flank as shown in Fig. 6.9. The phenomenon of stress concentrations can also be observed in both tooth edges.

6.4 Remarks

A computer program for generating the finite element analysis model has been developed. The finite element meshes, the definition of contacting surfaces and boundary conditions are automatically generated using the integrated computer program. The following advantages are evident: (1) The input file for finite element analysis models of the gear pair can be automatically generated for any rotational angle of pinion and gear obtained from TCA. A good stress convergence is assured because there is at least one contact point between the contact surfaces. (2) Generation of the finite element meshes is performed using the equation of tooth surfaces. The mesh density can be adjusted to meet specific requirements, and the nodes lying on the tooth surfaces are guaranteed to be the points on the real tooth surfaces of the pinion and the gear. Therefore, the accuracy of tooth profile coordinates in the FE model development can be obtained. (3) CAD computer program is not needed for generating the finite element analysis models.

The bearing contacts of the curvilinear-tooth gear pair with the applied torque have been discussed. Besides, the bending and contact stresses during the cycle of meshing are also investigated. The automatic generation of FEA models enables one to perform multi-tooth stress analysis. The analysis results show that the maximum contact stress and bending stress occur when the contact point is near the pitch point, and increasing the nominal radius R_c reduces the contact stresses and bending stresses due to a larger contact area of the gear tooth surface.

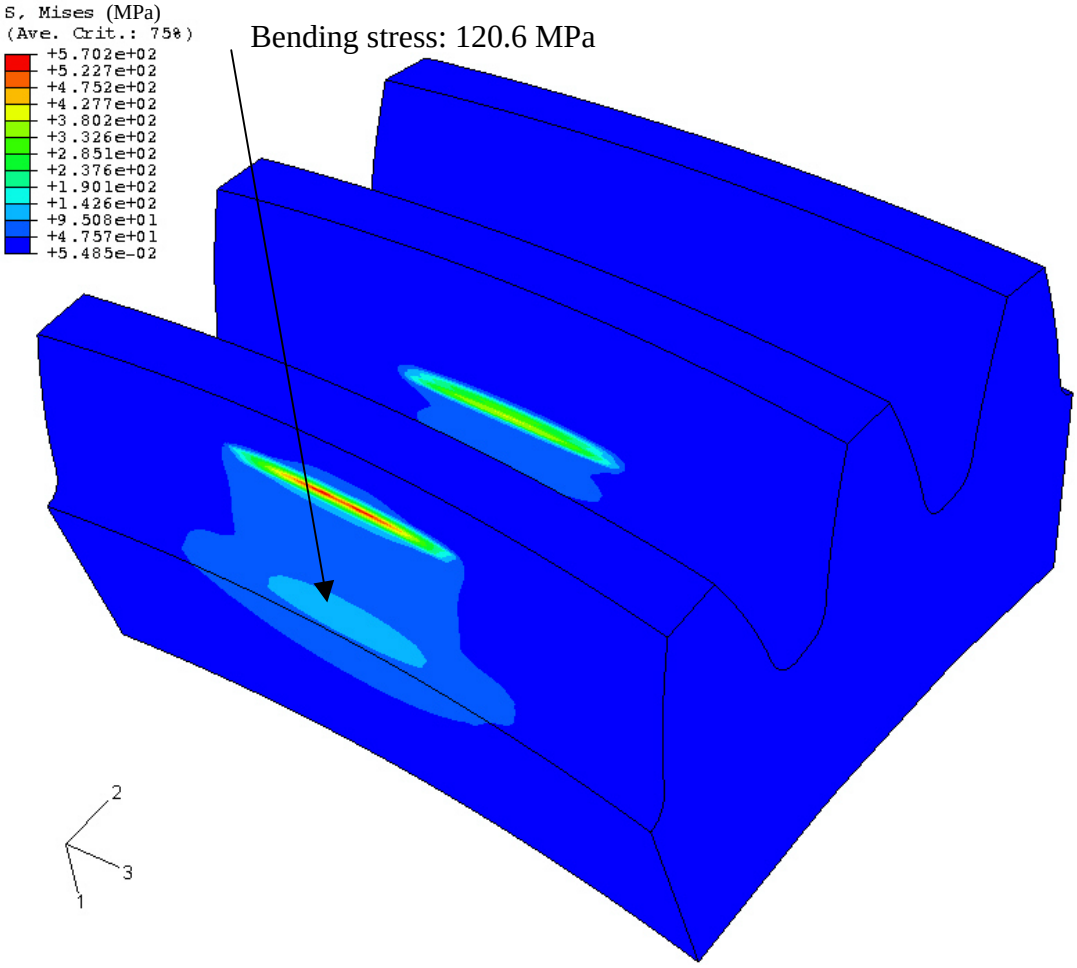

Fig. 6.3 Bearing contacts and stress distributions at beginning point of contact on the gear concave surfaces

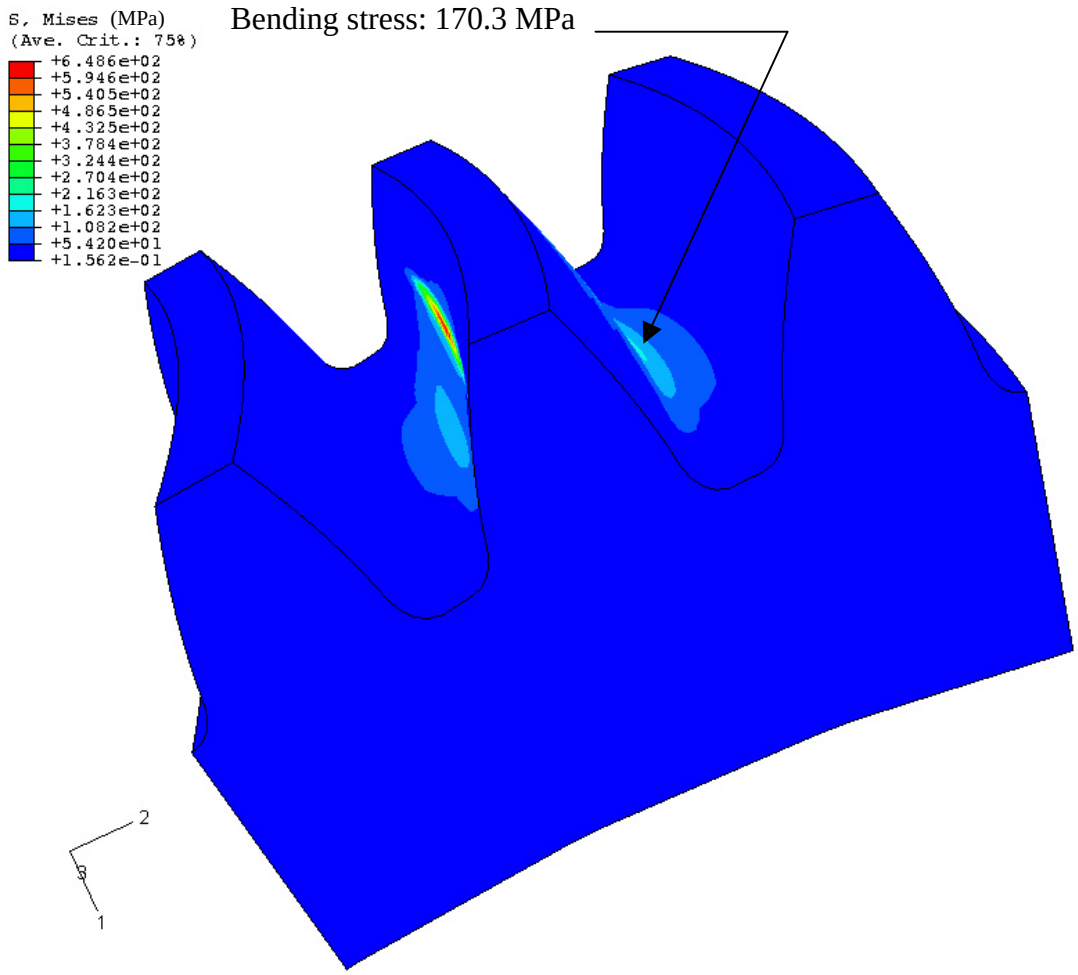

Fig. 6.4 Bearing contacts and stress distributions at the mean point of contact on the gear concave surfaces

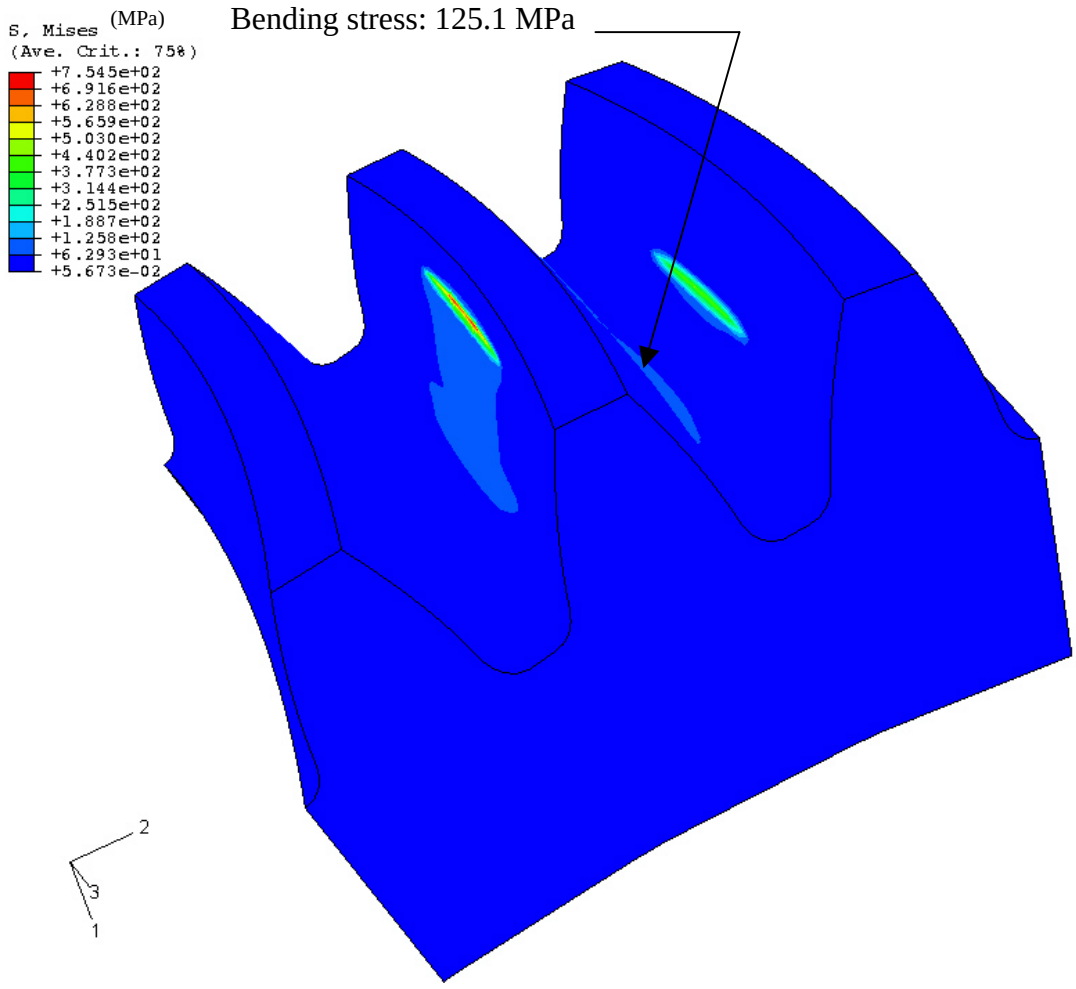

Fig. 6.5 Bearing contacts and stress distributions at the end point of contact on the gear concave surfaces

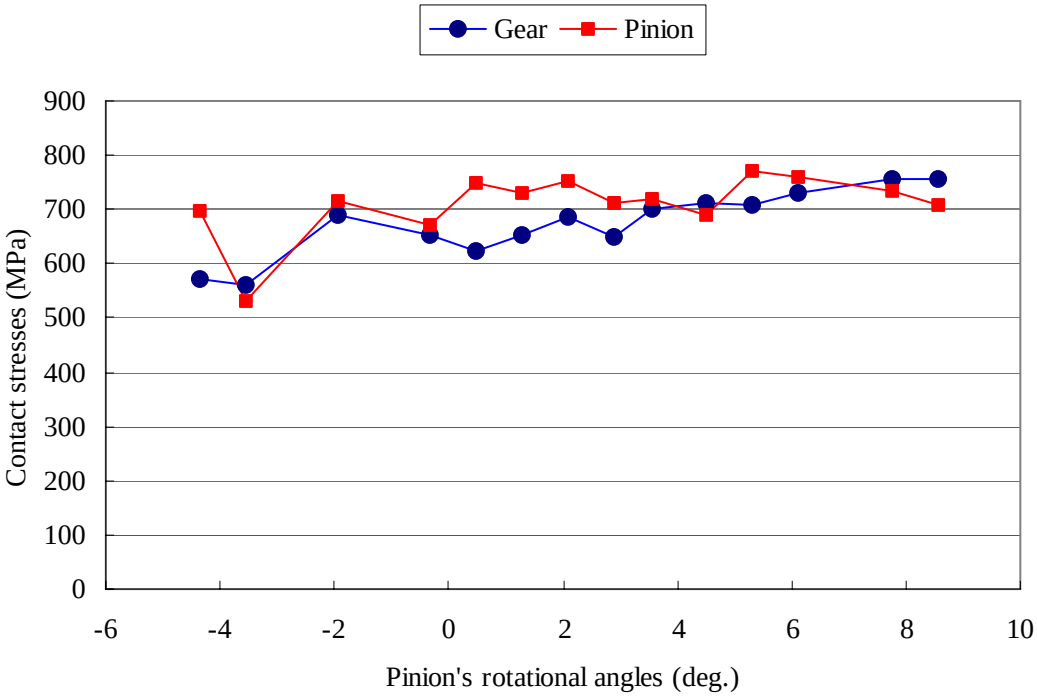

Fig. 6.6 Variations of contact stresses during one tooth of gear pair meshing

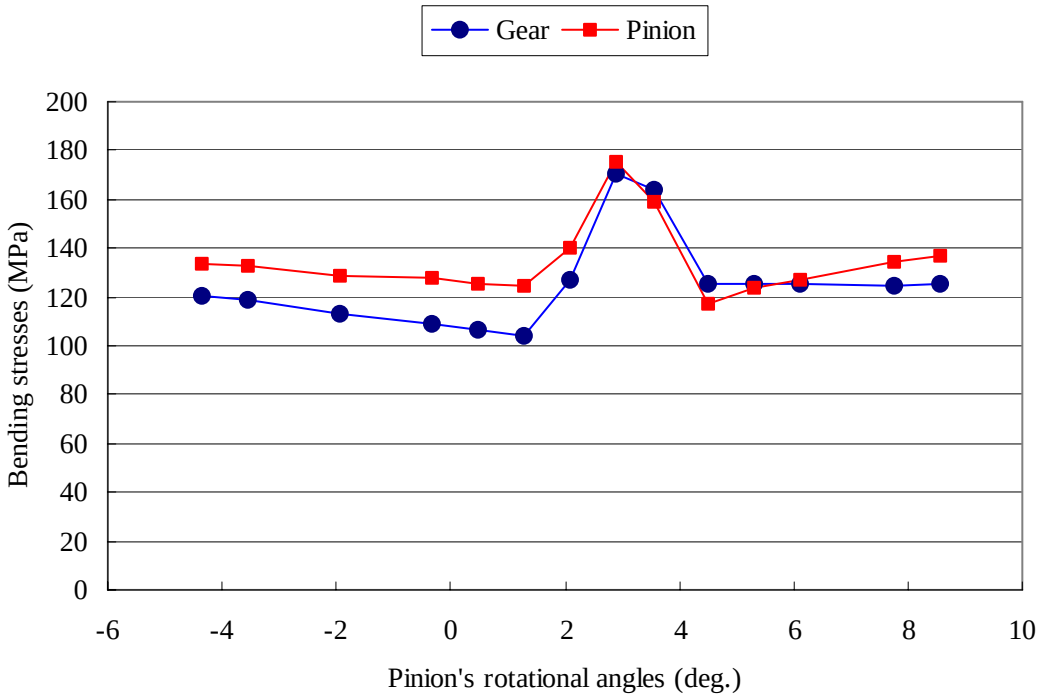

Fig. 6.7 Variation of bending stresses during one tooth of gear pair meshing

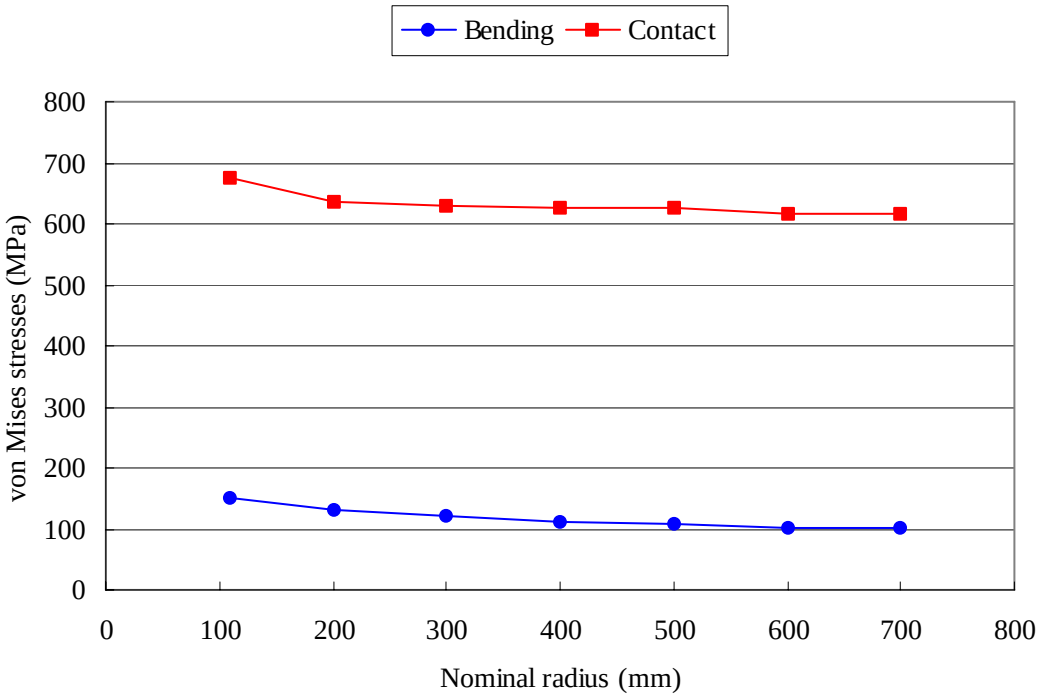

Fig. 6.8 Effects of nominal radius R_c on the maximum von Mises stress

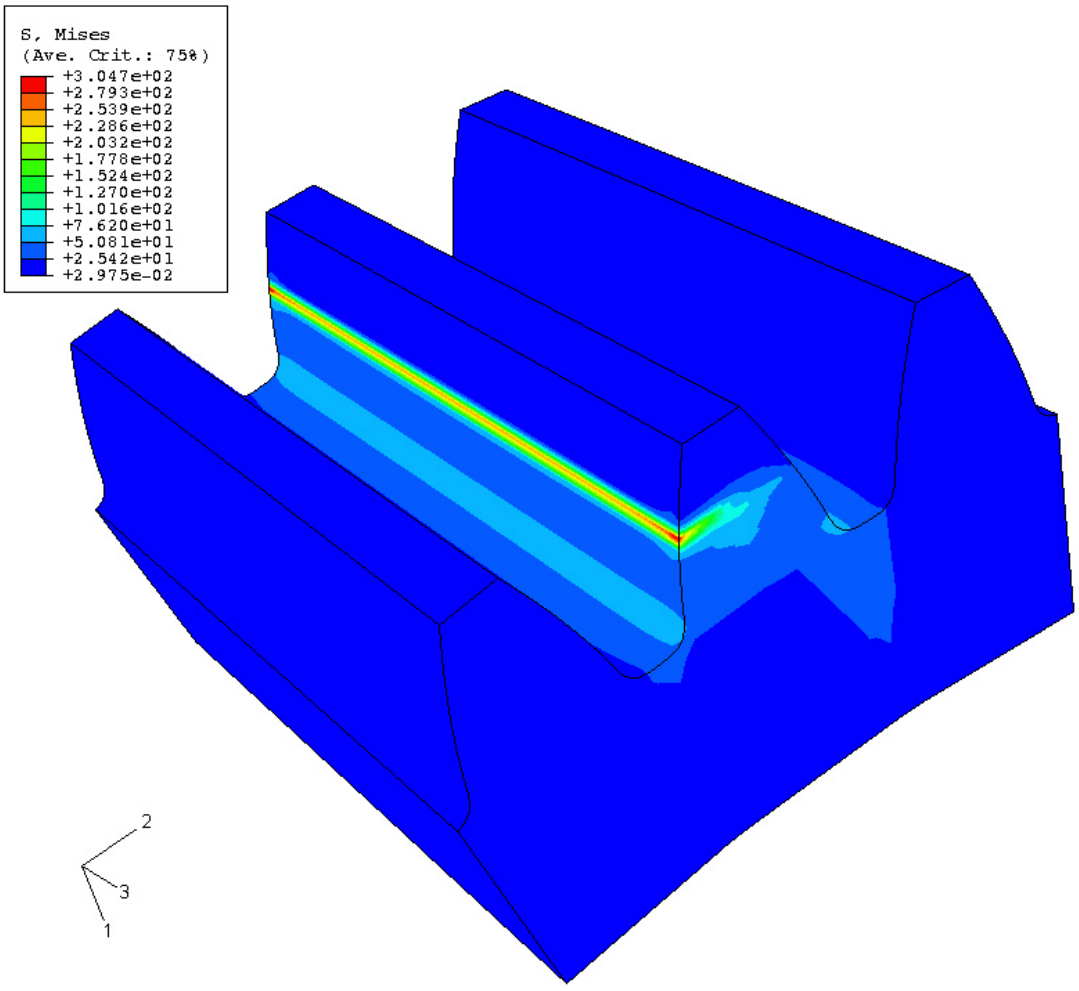

Fig. 6.9 Stress distributions on gear tooth surfaces as nominal radius R_c equals 50000 mm

CHAPTER 7

Conclusions and Future Work

In this study, the mathematical model of the curvilinear-tooth gear is developed, and the tooth undercutting and secondary cutting phenomena are also investigated as the curvilinear-tooth gear is generated. The procedure for calculation of principal curvatures and directions of the curvilinear-tooth surface is proposed and the corresponding calculation computer programs are also developed. The contact characteristics of the curvilinear-tooth gear pair such as bearing contacts, KEs and contact ellipses are investigated. Finally, the contact stress and bending stress are studied by applying finite element models with a pair of three-meshing-teeth gears.

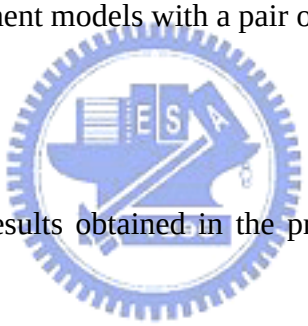

7.1 Conclusions

Based on the analysis results obtained in the previous chapters, the following conclusions are drawn:

(1) The mathematical model of curvilinear-tooth gears has been developed based on the cutting mechanism of a 6-axes CNC hobbing machine. The gear model is represented as a function of hob cutter's design parameters and the CNC generating motion parameters. The tooth profiles obtained by mathematical model can be considered as a standard profile for the curvilinear-tooth gears. The transverse gear chordal thickness measured at the middle section is larger than those of other sections, but the tooth thickness at the addendum circle in the middle section of face width is smaller than those of other sections.

(2) The kinematic method to find the differentiated equations of meshing is developed for analyzing tooth undercutting. According to the undercutting analysis results, the occurrence of tooth undercutting at the both-end sections of

face width of the curvilinear-tooth gear is much easier than other sections. The convex tooth surfaces compared with the concave tooth surfaces are much easier to undercut. The tooth undercutting of the curvilinear-tooth gears can be avoided with a large number of teeth or pressure angle, and the tooth undercutting may reduce by increasing the nominal radius of circular arc tooth trace. Owning to the geometric character of the hob cutter, the hob cutter with a larger outside diameter or a curvilinear-tooth gear with a smaller nominal radius of circular arc tooth trace will result in secondary tooth cutting when the curvilinear-tooth gears are generated by a hob cutter. Increasing the normal pressure angle or decreasing the outside diameter of the hob cutter can avoid secondary tooth cutting under the same nominal radius of circular arc tooth traces.

(3) An approach for the determination of principal curvatures and directions for the gear surface as an envelope to two-parameters family of hob cutter surfaces is developed. The proposed approach is the extension of Litvin's approach. Computer programs for calculations of the principal curvatures and directions of the tooth surfaces are developed.

(4) The curvilinear-tooth gear pair generated by a ZA worm-type hob cutter induces KEs when the gear pair is meshed under ideal assembly condition, or with center distance variations. However, the level of KEs of the gear pair is small. The bearing contacts are localized in the middle region of the tooth flank under ideal assembly condition. The KEs of the meshed gear pair under ideal assembly condition decreases when the gear pair is generated by a larger pitch radius of the hob cutter. The KE of the gear pair is not sensitive to axial misalignments because the contact type of the proposed curvilinear-tooth gear pair is in point contacts. The bearing contact can be localized near the middle region of the tooth flank by properly choosing a nominal radius of circular arc tooth trace. The ratio of the

major and minor axes of the contact ellipse is proportional to the nominal radius of circular arc tooth trace.

(5) A computer program for generating the finite element model is developed. The finite element meshes, the definition of contacting surfaces, and boundary conditions are automatically generated using the integrated computer program. The bearing contacts of the curvilinear-tooth gear pair under the applied torque is investigated. The analysis results show that the maximum bending stress occurs as the contact point is near the pitch point, and increasing the nominal radius R_c reduces the contact stresses and bending stresses due to a larger contact area of the gear tooth surface.

7.2 Future Work

The tooth surfaces of the curvilinear-tooth gear generated by a hob cutter are indeed new types of gear surfaces. Advanced studies of this kind of gear for industrial applications are important and necessary. In the future, the following research topics can be extended:

(1) The illustrated approach in Chapter 2 can be further extended to derive the mathematical model for noncircular face width gears, for example, parabolic or elliptical curved tooth traces.

(2) The sensitivity analysis can be used to study the surface deviation of the curvilinear-tooth gear with respect to machine-tool settings and the assembly errors of the hob cutter in the manufacturing process.

(3) Tooth surface deviations of the curvilinear-tooth gear having secondary cutting.

(4) Real contact ratio, load sharing between the meshing teeth, and transmission error under the given load may be implemented by considering multi-tooth finite element models. Moreover, the effect of friction force may be investigated by

defining the tooth surfaces interaction with friction.

(5) The single flank test and the measurement of noise and vibrations should be performed with the proposed curvilinear-tooth gear pairs.

REFERENCES

[1] Liu, S. T., "Curvilinear Cylindrical Gears," Gear Technology, May/ June, pp. 8-12, 1988.

[2] Dai, Y., Ariga, Y. and Nagata, S., "Study on A Cylindrical Gear with Curved Tooth Traces," Tenth World Congress on The Theory of Machine and Mechanisms, Vol. 6, pp. 2337-2342, Oulu, Finland, 1999.

[3] Andrei, L., Andrei, G., Epureanu, A., Oancea, N., and Walton, D., "Numerical Simulation and Generation of Curved Face Width Gears," International Journal of Machine Tools & Manufacture, Vol. 42, pp. 1-6, 2002.

[4] Tseng, R. T., and Tsay, C. B., "Mathematical Model and Undercutting of Cylindrical Gears with Curvilinear Shaped Teeth," Mechanism and Machine Theory, Vol. 36, pp. 1189-1202, 2001.

[5] Chang, S. L., Tsay, C. B. and Nagata, S., " A General Mathematical Model of Gears Cut by CNC Hobbing Machines," ASME J. of Mechanical Design, Vol. 119, pp. 108-113, 1997.

[6] Fang, H. S. and Tsay, C. B., "Mathematical Model and Bearing Contacts of the ZN-type Worm Gear Set Cut by Oversize Hob Cutters," Mechanism and Machine Theory, Vol. 35, pp. 1689-1708, 2000.

[7] Kim, D. H., "Geometry of Hob and Simulation of Generation of the Cylindrical Gears by Conventional or Climb Hobbing Operation," Proceedings of the Institution of Mechanical Engineers, Part D: Journal of Automobile Engineering, Vol. 215, No. 4, pp. 533-544, 2001.

[8] Litvin, F. L., and Seol, I. H., "Computerized Determination of Gear Tooth Surface as Envelope to Two Parameter Family of Surfaces," Computer Methods in Applied Mechanics and Engineering, Vol. 138, pp. 213-225, 1996.

[9] Kin, V., "Limitation of Worm and Worm Gear Surface in Order to Avoid Undercutting," Gear Technology, pp. 30-35, 1990.

[10] Fong, Z. H. and Tsay, C. B., "The Undercutting of Circular-Cut Spiral Bevel Gears," ASME J. of Mechanical Design, Vol. 114, pp. 317-325, 1992.

[11] Bair, B. W. and Tsay, C. B., "ZK-type Dual-Lead Worm and Worm Gear Drives: Geometry, " ASME J. of Mechanical Design, Vol. 120, pp. 414-421, 1998.

[12] Litvin, F. L., Theory of Gearing, NASA Publication RP-1212, Washington D.C., 1989.

[13] Litvin, F. L., Gear Geometry and Applied Theory, Prentice Hall, New Jersey, 1994.

[14] Litvin, F. L., Kin, V. and Zhang, Y., "Limitations of Conjugate Gear Tooth Surfaces," ASME J. of Mechanical Design, Vol. 112, pp. 230-236, 1990.

[15] Chang, S. L. and Tsay, C. B., "Computerized Tooth Profile Generation and Undercut Analysis of Noncircular Gears Manufactured with Shaper Cutters," ASME J. of Mechanical Design, Vol. 120, No.1, pp. 92-99, 1998.

[16] Liu, C. C. and Tsay, C.B., "Tooth Undercutting of Beveloid Gears," ASME J. of Mechanical Design, Vol. 123, pp. 569-576, 2001.

[17] Chen, Y. C. and Tsay, C. B., "Mathematical Model and Undercutting Analysis of Modified Circular-Arc Helical Gears," Journal of the Chinese Society of Mechanical Engineers, Vol. 22, pp. 41-51, 2001.

[18] Colbourne, J. R., "The Contact Stress in Novikov Gear," Mechanism and Machine Theory, Vol. 24, pp. 223-229, 1989.

[19] Evans, H. P. and Snidle, R. W., "Wildhaber-Novikov Circular Arc Gears: Elastohydrodynamics," ASME J. of Tribology, Vol. 115, pp. 487-492, 1993.

[20] Litvin, F. L.and Gutman Y., "A Method of Local Synthesis of Gears Grounded on the Connections Between the Principal and Geodetic Curvatures of Surfaces," ASME J. of Mechanical Design, Vol. 103, pp. 114-125, 1981.

[21] Colbourne, J. R., "The Curvature of Helicoids," Mechanism and Machine Theory, Vol. 39, pp. 905-919, 1989.

[22] Litvin, F. L., Chen, N. X., and Chen J. S., "Computerized Determination of Curvature Relations and Contact Ellipse for Conjugate Surfaces," Computer Methods in Applied Mechanics and Engineering, Vol. 125, pp. 151-170, 1995.

[23] Kang, Y. H. and Yan, H. S., "Curvature Analysis of Variable Pitch Lead Screws with Cylindrical Meshing Elements," Transactions of the Canadian Society for Mechanical Engineering, Vol. 20, pp. 139-157, 1996.

[24] Yan, H. S. and Cheng, W. T., "Curvature Analysis of Spatial Cam-Follower Mechanisms," Mechanism and Machine Theory, Vol. 34, pp. 319-339, 1999.

[25] Tsay, C. B., "Helical Gears with Involute Shaped Teeth: Geometry, Computer Simulation, Tooth Contact Analysis and Stress Analysis," ASME J. of Mechanical Design, Vol. 110, No. 4, pp. 482-491, 1988.

[26] Liu, C. C. and Tsay, C.B., "Contact Characteristics of Beveloid Gears," Mechanism and Machine Theory, Vol. 37, pp. 333-350, 2002.

[27] Tseng, R. T. and Tsay, C. B., "Contact Characteristics of Cylindrical Gears with Curvilinear shaped teeth," Mechanism and Machine Theory, Vol. 39, pp. 905-919, 2004.

[28] Litvin, F. L., Zhang, J., Handschuh, R. F. and Coy, J. J., "Topology of Modified Helical Gears," Surface Topography, pp. 41-58, 1989.

[29] Litvin, F. L., Seol, I. H., Kim, D., Lu, J., Wang, G. A., Egelja, A., Zhao, X., and Handschuh, R. F., "Kinematic and Geometric Models of Gear Drives," ASME J. of Mechanical Design, Vol. 118, pp. 544-550, 1996.

[30] Litvin, F. L., Chen, N. X., Hsiao, C. L. and Handschuh, R. F., "Generation of Helical Gears with New Surfaces Topology by Application of CNC Machines," Gear Technology, pp. 30-33, 1994.

[31] Litvin, F. L., Chen, N. X., Lu. J. and Handschuh, R. F., "Computerized Design and Generation of Low-Noise Helical Gears with Modified Surface Topology," ASME Journal of Mechanical Design, Vol. 117, pp. 254-261, 1995.

[32] Litvin, F. L. and Kim, D. H., "Computerized Design, Generation and Simulation of Modified Involute Spur Gears with Localized Bearing Contact and Reduced Level of Transmission Errors," ASME Journal of Mechanical Design, Vol. 119, pp. 96-100, 1997.

[33] Chen, Y. C. and Tsay, C. B., "Tooth Contact Analysis and Kinematic Optimization of a Modified Helical Gear Pair with Involute-Teeth Pinion and Modified-Circular-Arc Gear," Journal of the Chinese Society of Mechanical Engineers, Vol. 21, pp. 537-547, 2000.

[34] Fong, Z. H. and Tsay, C. B., "Kinematical Optimization of Spiral Bevel Gears," ASME J. of Mechanical Design, Vol. 114, pp. 498-506, 1992.

[35] Chang, S. L., Tsay, C. B. and Tseng, C. H., "Kinematic Optimization of a Modified Helical Gear Train," ASME J. of Mechanical Design, Vol. 119, pp. 307-314, 1997.

[36] Zhang, Y. and Fang, Z., "Analysis of Transmission Errors Under Load of Helical Gears with Modified Tooth Gears," ASME J. of Mechanical Design, Vol. 119, pp. 120-126, 1997.

[37] Zhang, Y. and Fang, Z., "Analysis of Tooth Contact and Load Distribution of Helical Gears with Crossed-Axes," Mechanism and Machine Theory, Vol. 34, pp.

41-57, 1999.

[38] Umeyama, M., Kato, M. and Inoue, K., “Effects of Gear Dimensions and Tooth Surface Modifications on the Loaded Transmission Error of a Helical Gear Pair,” ASME J. of Mechanical Design, Vol. 120, pp. 119-125, 1998.

[39] Janninck, W. L., “Contact Surface Topology of Worm Gear Teeth,” Gear Technology, March/April, pp. 31-47, 1988.

[40] Chen, W. H. and Tsai, P., “Finite Element Analysis of an Involute Gear Drive Considering Friction Effects,” ASME Journal of Engineering for Industry, Vol. 111, pp. 94-111, 1989.

[41] Ganesan, N. and Vijayarangan, S., “Static Contact Stress Analysis of a Spur Gear Tooth Using the Finite Element Method, Including Frictional Effects,” Computers and Structures, Vol. 51, pp. 765-770, 1994.

[42] Simon, V., “FEM Stress Analysis in Hypoid Gears,” Mechanism and Machine Theory, Vol. 35, pp. 1197-1220, 2000.

[43] Simon, V., “Stress Analysis in Double Enveloping Worm Gears by Finite Element Method,” ASME Journal of Mechanical Design, Vol. 115, pp. 179-185, 1993.

[44] Tsay, C. B. and Fong, Z. H., “Computer Simulation and Stress Analysis of Helical Gears with Pinion Circular Arc and Gear Involute Teeth,” Mechanism and Machine Theory, Vol. 26, pp. 145-154, 1991.

[45] Litvin, F. L., Chen, J. S., Lu, J. and Handschuh, R. F., “Application of Finite Element Analysis for Determination of Load Share, Real Contact Ratio, Precision of Motion, and Stress Analysis,” ASME Journal of Mechanical Design, Vol. 118, pp. 561-567, 1996.

[46] Filiz, I. H. and Eyercioglu, O., “Evaluation of Gear Tooth Stresses by a Finite Element Meshing Simulation,” ASME Journal of Engineering for Industry, Vol. 117, pp. 232-239, 1995.

[47] Bibel, G. D., Kumar, A., Reddy, S. and Handschuh, R., “Contact Stress Analysis of Spiral Bevel Gears Using Finite Element Analysis,” ASME Journal of Mechanical Design, Vol. 117, pp. 235-240, 1995.

[48] Bibel, G. D. and Handschuh, R., “Meshing of a Spiral Bevel Gear Set With 3-D Finite Element Analysis,” Gear Technology, March/April, pp. 44-47, 1997.

[49] Celik, M., “Comparison of Three Teeth and Whole Body Models in Spur Gear

Analysis," Mechanism and Machine Theory, Vol. 34, pp. 1227-1235, 1999.

[50] Litvin, F. L., Fuentes, A., Fan, Q. and Handschuh, R. F., "Computerized Design, Simulation of Meshing, and Contact Stress Analysis of Face-Milled Formate Generated Spiral Bevel Gears," Mechanism and Machine Theory, Vol. 37, pp. 441-459, 2002.

[51] Chen, Y. C. and Tsay, C. B., " Stress Analysis of a Helical Gear Set with Localized Bearing Contact," Finite Elements in Analysis and Design, Vol. 38, No. 8 pp. 707-723, 2002.

[52] Barone, S., Borgianni, L. and Forte, P., "Evaluation of the Effect of Misalignment and Profile Modification in Face Gear Drive by a Finite Element Meshing Simulation," ASME Journal of Mechanical Design, Vol. 126, pp. 916-924, 2004.

[53] Handschuh, R. F. and Bibel, G. D., "Experimental and Analytical Study of Aerospace Spiral Bevel Gear Tooth Fillet Stresses," ASME Journal of Mechanical Design, Vol. 121, pp. 565-572, 1999.

[54] Li, S., "Gear Contact Model and Loaded Tooth Contact Analysis of a Three-Dimensional, Thin-Rimmed Gear," ASME Journal of Mechanical Design, Vol. 124, pp. 511-517, 2002.

[55] Townsend, D. P., Dudley's Gear Handbook, 2nd Edition, McGraw-Hill, New York, 1992.

[56] Nutbourne, A. W., and Martin, R. R., Differential Geometry Applied to Curve and Surface Design, Vol. 1, Ellis Horwood Limited, Chichester, England, 1988.

[57] Hibbitt, Karlsson & Sorensen, ABAQUS/Standard 6.2, User's Manual, U.S.A., 2001.